A Minimal Three-Dimensional Tropical Cyclone Model

HONGYAN ZHU, ROGER K. SMITH, AND WOLFGANG ULRICH

Meteorological Institute, University of Munich, Munich, Germany

ABSTRACT

A minimal 3D numerical model designed for basic studies of tropical cyclone behavior is described. The model is formulated in σ coordinates on an f or β plane and has three vertical levels, one characterizing a shallow boundary layer and the other two representing the upper and lower troposphere, respectively. It has three options for treating cumulus convection on the subgrid scale and a simple scheme for the explicit release of latent heat on the grid scale. The subgrid-scale schemes are based on the mass-flux models suggested by Arakawa and Ooyama in the late 1960s, but modified to include the effects of precipitation-cooled downdrafts. They differ from one another in the closure that determines the cloud-base mass flux. One closure is based on the assumption of boundary layer quasi-equilibrium proposed by Raymond and Emanuel.

It is shown that a realistic hurricane-like vortex develops from a moderate strength initial vortex, even when the initial environment is slightly stable to deep convection. This is true for all three cumulus schemes as well as in the case where only the explicit release of latent heat is included. In all cases there is a period of gestation during which the boundary layer moisture in the inner core region increases on account of surface moisture fluxes, followed by a period of rapid deepening. Precipitation from the convection scheme dominates the explicit precipitation in the early stages of development, but this situation is reversed as the vortex matures. These findings are similar to those of Baik et al., who used the Betts–Miller parameterization scheme in an axisymmetric model with 11 levels in the vertical. The most striking difference between the model results using different convection schemes is the length of the gestation period, whereas the maximum intensity attained is similar for the three schemes. The calculations suggest the hypothesis that the period of rapid development in tropical cyclones is accompanied by a change in the character of deep convection in the inner core region from buoyantly driven, predominantly upright convection to slantwise forced moist ascent.

1. Introduction

Numerical models of tropical cyclones have played and continue to play an important role in enhancing our understanding of tropical-cyclone dynamics. Single-layer, barotropic models have been used extensively to study tropical-cyclone motion (see, e.g., Elsberry 1995), but baroclinic multilayer models with some representation of moist processes are required to study other aspects, such as the intensification of tropical cyclones, their mature structure and energetics, and their interaction with other atmospheric systems as well as the ocean. The development of tropical-cyclone models has had a long history, a seminal paper being that of Ooyama (1969). The early models, including Ooyama's, were mostly axisymmetric and had limited vertical resolution, although some experiments with asymmetric models were reported in the early 1970s (e.g., Anthes et al. 1971a,b; Anthes 1972; Kurihara and Tuleya 1974; Madala and Piacsek 1975). Ooyama's model is perhaps one of the simplest to have been developed that includes moist processes. It has three homogeneous layers of air representing the upper and lower free troposphere and a shallow boundary layer. The effects of deep moist convection are represented in terms of a mass (and momentum) transfer from the boundary layer and middle layer into the upper layer, the amount of mass transferred from the middle layer being determined on the basis of thermodynamic considerations involving a simple cloud model. As computer power increased, the resolution of models increased also, both in the horizontal and vertical. Indeed, some authors dispensed entirely with an implicit representation (or parameterization) of deep moist convection in preference to an explicit representation of latent heat release, coupled with a crude representation of cloud microphysics (typically the conversion of cloud water to rainwater) (see, e.g., Yamasaki 1975, 1977; Rosenthal 1978; Jones 1977, 1980; Willoughby et al. 1984; Rotunno and Emanuel 1987). Today, computer power is such that calculations using quite complex models with a relatively high horizontal and vertical resolution and sophisticated representations of physical processes can be carried out, although many models still use some form of cumulus parameterization

Corresponding author address: Prof. Roger K. Smith, Meteorological Institute, University of Munich, Theresienstr. 37, 80333 Munich, Germany.
E-mail: roger@meteo.physik.uni-muenchen.de

scheme. Such models are used operationally by numerous weather services for weather prediction including the prediction of tropical cyclones.

Despite the technological progress, there remains a role for simple models, the results from which are usually easier to interpret than those from models with complex representations of physical processes. Indeed, much insight into tropical-cyclone behavior has emerged from simple models. Noteworthy examples of such models include the axisymmetric steady-state model of Emanuel (1986) and the axisymmetric time-dependent models of Ooyama (1969), DeMaria and Pickle (1988), and Emanuel (1989, 1995a). The last two models by Emanuel include new representations of moist convection, which reflect recent advances in our understanding of convective processes (see, e.g., Smith 1997).

A review of methods that have been used to represent moist processes in tropical-cyclone models is given by Smith (2000). Many of the parameterization schemes used previously have been of the Kuo-type (Kuo 1965, 1974) in which the closure is based on the resolved-scale moisture convergence. These types of schemes have come under much criticism in recent years (Emanuel and Raymond 1993; Emanuel 1994; Emanuel et al. 1994) and it follows that deductions from models that use them must be viewed with some caution. Alternative schemes have been implemented in multilevel, axisymmetric models by Wada (1979), who used the Arakawa–Schubert scheme (Arakawa and Schubert 1974), and Baik et al. (1990a,b), who used the Betts–Miller scheme (Betts 1986). Many models allow saturation to occur on the grid-scale if this is called for, notable exceptions being those of Ooyama (1969) and its derivatives (see, e.g., Smith 2000 and references therein) and those of Emanuel cited above, none of which have a separate integrated water budget.

The use of homogeneous layers of constant density in Ooyama's (1969) model and the consequent lack of internal energy is an obstacle to relating the energy conversions in the model to those in real hurricanes (Ooyama 1969, p. 25). As a result, the rate of latent heat release is not equal to the rate at which potential energy (generated by the mass transfer between layers) is converted to kinetic energy (Ooyama 1969, section 12). DeMaria and Pickle (1988) circumvented this difficulty by a reformulation in terms of three layers of uniform potential temperature, but they also do not allow saturation to occur on the grid scale. Most tropical-cyclone models settle for a particular cumulus parameterization scheme, but we are aware of only one study in which different schemes have been compared when used in the same model. The exception is the paper by Baik et al. (1991), who compare the Betts–Miller and Kuo schemes in a multilevel axisymmetric model.

The aim of the present work is to develop a minimal three-dimensional tropical-cyclone model with a fully integrated representation of moist physics that is suitable for basic studies of tropical-cyclone behavior. Furthermore we seek to compare different convection schemes in the model to determine whether important features of cyclone evolution are sensitive to the use of a particular scheme. We investigate three schemes based on the formulation suggested by Arakawa (1969) and examine also the case in which moist processes are represented only on the resolvable scale. The convection schemes differ only in the closure used to determine the cloud-base mass flux and are essentially modifications of the schemes used by Arakawa himself, Ooyama (1969), and Emanuel (1995a). Modifications of the Arakawa and Ooyama schemes reflect the inclusion of precipitation-cooled downdrafts, while more major modifications of Emanuel's scheme were called for. Both the 1989 and 1995 Emanuel schemes are designed for an axisymmetric model and assume slantwise neutrality to moist convection in the troposphere. The elegant formulation in potential radius coordinates circumvents the need to consider a separate outflow layer in the upper troposphere, as this is implicit in the coordinate transformation. Moreover, the assumption of slantwise neutrality constrains the dynamics and thermodynamics above the boundary layer. The generalization of the scheme to three dimensions requires substantial modification as potential radius is then inconvenient to use and its avoidance necessitates the introduction of an outflow layer.

In section 2 we describe the model and in section 3 the cumulus parameterization schemes. The four calculations examined in this paper are detailed in section 4 and the results of these are described in section 5. A discussion of issues emerging from the results forms the basis of section 6, and section 7 follows with a critical appraisal of the model. A summary and the conclusions are given in section 8.

2. Description of the model

a. Governing equations

The model is based on the three-dimensional hydrostatic primitive equations in sigma coordinates (x, y, σ) on an f plane or β plane, where x and y are in the zonal and meridional directions, respectively, and

$$\sigma = \frac{p - p_{\text{top}}}{p_s - p_{\text{top}}} = \frac{p - p_{\text{top}}}{p^*}, \qquad (1)$$

where $p^* = p_s - p_{\text{top}}$, p_s, and p_{top} are the surface and top pressures, and p_{top} is a constant, taken here to be 100 mb. Then the upper and lower boundary conditions require that $\dot{\sigma} = 0$ at $\sigma = 0$ and $\sigma = 1$, where $\dot{\sigma} = D\sigma/Dt$ is the "vertical" σ velocity and D/Dt is the material derivative. The zonal and meridional momentum equations and the hydrostatic equation are

$$\frac{\partial u}{\partial t} = -\left(u\frac{\partial u}{\partial x} + v\frac{\partial u}{\partial y}\right) - \dot{\sigma}\frac{\partial u}{\partial \sigma} + fv$$

$$- \frac{R\theta\sigma(p^*\sigma + p_{\text{top}})^{\kappa-1}}{p_o^\kappa}\frac{\partial p^*}{\partial x} - \frac{\partial \Phi}{\partial x} + D_u, \quad (2)$$

$$\frac{\partial v}{\partial t} = -\left(u\frac{\partial v}{\partial x} + v\frac{\partial v}{\partial y}\right) - \dot{\sigma}\frac{\partial v}{\partial \sigma} - fu$$

$$- \frac{R\theta\sigma(p^*\sigma + p_{\text{top}})^{\kappa-1}}{p_o^\kappa}\frac{\partial p^*}{\partial y} - \frac{\partial \Phi}{\partial y} + D_v, \quad (3)$$

$$\frac{\partial \Phi}{\partial \sigma} = -\frac{Rp^*(p^*\sigma + p_{\text{top}})^{\kappa-1}}{p_o^\kappa}\theta, \quad (4)$$

where u and v are the velocity components in the x and y directions; $f = f_o + \beta y$ is the Coriolis parameter; f_o and $\beta = df/dy$ are constants; R is the specific gas constant for dry air; $\kappa = R/c_p$; c_p is the specific heat of dry air; θ is the potential temperature; Φ is the geopotential; D_u and D_v represent the frictional drag in the x and y directions, respectively (see section 2d); and $p_o = 1000$ mb. In this paper, the calculations are carried out on an f plane at 20°N whereupon β is set to zero. The surface pressure tendency equation, derived from the continuity equation[1] and boundary conditions is

$$\frac{\partial p^*}{\partial t} = -\int_0^1 \left(\frac{\partial(p^*u)}{\partial x} + \frac{\partial(p^*v)}{\partial y}\right) d\sigma \quad (5)$$

and $\dot{\sigma}$ is given by

$$\dot{\sigma} = -\frac{1}{p^*}\int_0^\sigma \left(\frac{\partial(p^*u)}{\partial x} + \frac{\partial(p^*v)}{\partial y}\right) d\sigma$$

$$+ \frac{\sigma}{p^*}\int_0^1 \left(\frac{\partial(p^*u)}{\partial x} + \frac{\partial(p^*v)}{\partial y}\right) d\sigma. \quad (6)$$

The thermodynamic and moisture equations are

$$\frac{\partial \theta}{\partial t} = -\left(u\frac{\partial \theta}{\partial x} + v\frac{\partial \theta}{\partial y}\right) - \dot{\sigma}\frac{\partial \theta}{\partial \sigma} + Q_\theta, \quad \text{and} \quad (7)$$

$$\frac{\partial q}{\partial t} = -\left(u\frac{\partial q}{\partial x} + v\frac{\partial q}{\partial y}\right) - \dot{\sigma}\frac{\partial q}{\partial \sigma} + Q_q, \quad (8)$$

where q is the specific humidity, Q_θ is the diabatic heat source, and Q_q is the moisture source, the last two of which include contributions from surface fluxes (section 2d) and deep cumulus convection (section 2d). The temperature T is related to θ by

$$T = \left(\frac{p}{p_o}\right)^\kappa \theta = \frac{(p^*\sigma + p_{\text{top}})^\kappa}{p_o^\kappa}\theta. \quad (9)$$

_____

[1] In σ coordinates, the continuity equation takes the differential form: $\partial p^*/\partial t + \partial(p^*u)/\partial x + \partial(p^*v)/\partial y + \partial(p^*\dot{\sigma})/\partial \sigma = 0$.

b. Explicit moist processes

Explicit condensation is treated in a similar way to Baik et al. (1990a), but the procedure is simpler here because of the coarser vertical resolution used. If at any time the air becomes supersaturated at a grid point, the specific humidity is set equal to the saturation specific humidity and the excess water vapor is condensed to liquid water. This water is assumed to precipitate out while the latent heat released is added to the air. The latent heat raises the air temperature and thereby the saturation specific humidity, requiring a further adjustment of the amount of condensed water, and so on. Accordingly, it is necessary to iterate to determine the final amount of condensed water and latent heat release, but the number of iterations required is small. Like Baik et al. (1990a), we apply this explicit procedure before the subgrid-scale convection scheme.

c. Radiative cooling

A Newtonian cooling term, $-(\theta - \theta_{\text{ref}})/\tau_R$, is added to the right hand side of the thermodynamic equation to crudely represent the effect of radiative cooling. In this expression θ_{ref} is the initial potential temperature profile of the basic state and τ_R is a radiative timescale. Following Emanuel (1989, p. 3436) we take τ_R to be 12 h. However, we do not apply this cooling where the relative humidity in layer 3 is larger than 90%. This is a rough attempt to account for the differential cooling rate between clear and cloudy air.

d. Surface turbulent fluxes

The turbulent flux of momentum to the sea surface and the fluxes of water vapor and sensible heat at the surface are represented by bulk aerodynamic formulas in the form

$$(F_u, F_v) = -\rho C_d|\mathbf{u}_b|(u_b, v_b),$$

$$F_q = \rho C_h|\mathbf{u}_b|(q_s^* - q_b),$$

$$F_{\text{SH}} = \rho c_p C_h|\mathbf{u}_b|(T_s - T_b), \quad (10)$$

where the subscript "b" denotes the value at the middle of the boundary; $\mathbf{u}_b = (u_b, v_b)$; T_s and q_s^* are the sea surface temperature and saturated specific humidity at this temperature, respectively; ρ is the near-surface air density; C_D is the surface drag coefficient; and C_h is the bulk transfer coefficient for heat and moisture. The quantity q_s^* depends also on the sea surface pressure. Here we set ρ equal to the mean density of the lower layer, ρ_b, and assume that $C_h = C_D$, with C_D calculated from the formula used by Shapiro (1992):

$$C_D = (1.024 + 0.05366 \, R_F \, |\mathbf{u}_b|) \times 10^{-3}, \quad (11)$$

where $R_F = 0.8$ is used to reduce the boundary layer wind, $\mathbf{u}_b$ to the 10-m level. The assumption that $C_D = C_h$ is simply expedient in view of the current lack of

knowledge on how these quantities are related in high wind speeds. Emanuel (1995b) presents circumstantial evidence to suggest that the ratio C_D/C_h lies in the range 0.75–1.5. The sensitivity of our calculations to this ratio will be included in a separate study.

The frictional drag terms D_u and D_v in Eqs. (2) and (3) are obtained by dividing the corresponding terms F_u and F_v in Eq. (10) by the depth z_b and the density ρ_b of the lower layer. Similarly the contributions to the source terms Q_θ and Q_q in Eqs. (7) and (8) from the terms F_{SH} and F_q in Eqs. (10) are given by the relations: $Q_\theta = F_{SH}/(\rho_b c_p \pi_s z_b)$ and $Q_q = F_q/\rho_b z_b$, where $\pi_s = (p_s/p_o)^\kappa$ is the Exner function at the surface.

e. Boundary and initial conditions

The calculations are carried out in a zonal channel with rigid walls at $y = \pm Y$ and periodic boundary conditions at $x = \pm X$. It is assumed that there is no motion normal to the meridional boundaries (i.e., $v = 0$ at $y = \pm Y$) and that meridional gradients are zero at these boundaries [i.e., $\partial(u, \theta, q)/\partial y = 0$ at $y = \pm Y$]. Surface pressure and geopotential are adjusted geostrophically to satisfy the equation

$$\frac{\sigma}{\rho}\frac{\partial p_s}{\partial y} + \frac{\partial \Phi}{\partial y} = -fu. \qquad (12)$$

The initial axisymmetric vortex is barotropic and has the same tangential velocity distribution as that used by Smith et al. (1990) given by

$$v(r') = \frac{av_m r'(1 + br'^4)}{(1 + cr'^2 + dr'^6)^2}, \qquad (13)$$

where $r' = r/r_m$, r is the radius from the vortex center, r_m is the radius of maximum tangential wind speed v_m, and a, b, c, and d are constants, where $a = 1.78803$, $b = 4.74736 \times 10^{-3}$, $c = 0.339806$, and $d = 5.37727 \times 10^{-4}$. Here we choose $v_m = 15$ m s^{-1}, and $r_m = 120$ km. The computational domain size is 4000 km $\times$ 4000 km and the grid resolution is 20 km.

The initial mass and geopotential fields are obtained by solving the inverse balance equation, which takes the form (Kurihara and Bender 1980),

$$\nabla^2\Phi + \nabla\left(\frac{RT\sigma}{p}\nabla p*\right) = 2J(u,v) + f\zeta - \beta u, \qquad (14)$$

where J is the Jacobian operator. The temperature is obtained from the hydrostatic equation (4). At $\sigma = 1$, where $\Phi_s = 0$, the equation can be written as

$$\nabla(RT_s\nabla \ln p_s) = 2J(u_s, v_s) + f\zeta_s - \beta u_s, \qquad (15)$$

where the subscript "s" denotes the surface value of the relevant quantity. This equation can be solved for the surface pressure field if the surface temperature is known. In the calculations described in this paper, $\beta = 0$.

The far-field temperature and humidity structure are based on the mean West Indies sounding for the hur-
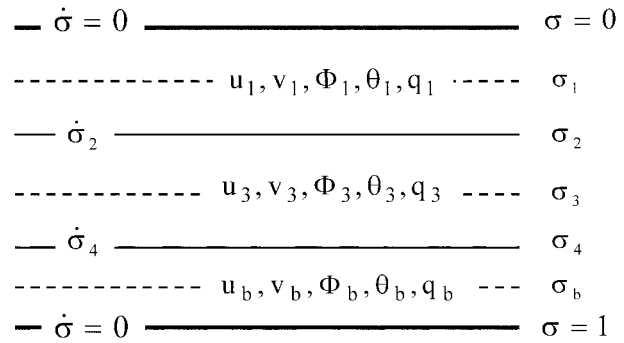
FIG. 1. Configuration of σ levels in the model showing locations where the dependent variables are stored. The horizontal velocity components, geopotential, potential temperature, specific humidity, and the moist static energy used in the convection scheme (see section 3) are calculated at levels 1, 3 and b, and the vertical velocity $\dot\sigma$ and convective mass flux are stored at levels 2 and 4.

ricane season (Jordan 1957), but the near-surface specific humidity has been reduced slightly so that the sounding is initially stable to deep convection (see appendix a). The environment surface pressure is 1015 mb, and the minimum surface pressure at the vortex center is initially 1008 mb. Horizontal variations of specific humidity in the presence of the initial vortex are neglected. The sea surface temperature is taken to be 28°C.

f. Subgrid-scale diffusion

To filter out the energy in high-frequency waves, a fourth-order horizontal diffusion term $D_4 = -k_1\nabla_h^4\chi$ is added to all prognostic equations with a diffusion coefficient $k_1 = 0.0008\Delta^4$, where ∇_h is the horizontal Laplacian operator and Δ is the horizontal grid spacing. At the boundaries, a second-order diffusion term $D_2 = k_2\nabla_h^2\chi$ is applied with $k_2 = 0.0008\Delta^2$. The philosophy of such an approach is discussed by Pielke (1984, see section 10.6).

g. The numerical method

The model is divided vertically into three unequally deep layers with boundaries at $\sigma = 0$, σ_2, σ_4, and $\sigma = 1$ (see Fig. 1). All the dependent variables, such as horizontal velocity, potential temperature, specific humidity, and geopotential, are defined in the middle of each layer ($\sigma = \sigma_1$, σ_3, and σ_b), and $\dot\sigma$ is staggered, that is, it is defined at the boundaries between layers. The equations are expressed in finite-difference form in both the horizontal and vertical and integrated forward in time using the Adams–Bashforth third-order method.

The initial pressure, temperature, specific humidity, and geopotential height in the middle of each layer and at the boundaries between layers are detailed in appendix a, Table A1.
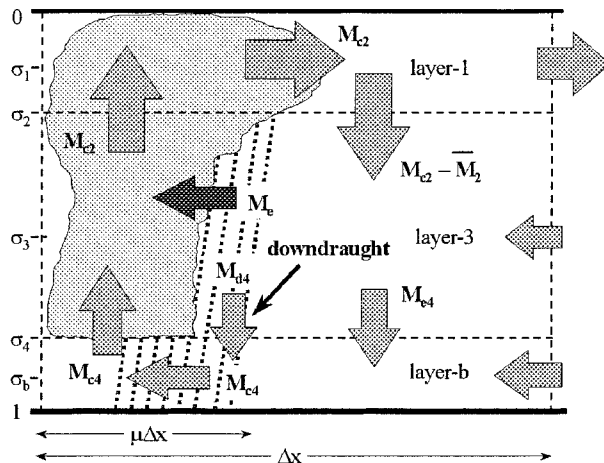
FIG. 2. Schematic diagram of the vertical circulation within a grid column in the cumulus parameterization schemes used in this paper. The schemes are based on a steady-state bulk cloud model, which is assumed to occupy a small fraction μ of the grid box. The cloud takes mass from the boundary layer at a rate M_{c4} and detrains it to the upper layer at a rate M_{c2}. Entrainment of middle-layer air into the cloud takes place along the way at a rate M_e, just sufficient to ensure that the air detrains from the cloud at the same temperature as the environment at level 1 (i.e., detrainment of cloud air occurs at its level of neutral buoyancy). The downdraft mass flux M_{d4} is assumed to be proportional to M_{c4} and the downdraft is considered to be a part of the cloud environment. The resolved-scale flow in or out of the grid box is indicated in the diagram by arrows through the right boundary. The resolved-scale vertical mass fluxes are denoted by $\overline{M}_n$ ($n = 2, 4$) and the clear air mass flux at level 4 is denoted by M_{e4} (by clear air we mean the part of the cloud environment where there is no precipitation). If $\overline{M}_n$ is less than the *net* mass flux, $M_{cn} - M_{dn}$, associated with convection at a particular level, there is subsidence in the clear air (e.g., $M_{e4} > 0$) which warms and dries the cloud environment in the layer below.

3. Cumulus parameterization schemes

There are three different options in the model for representing subgrid-scale deep cumulus convection. The first is a modified version of the scheme proposed by Arakawa (1969). In its original form, the scheme is similar to that proposed by Ooyama (1969), but is more general because the thermodynamic equation is included directly in the formulation, whereas in Ooyama's model the dynamics and thermodynamics are coupled only through the specification of the mass transfer between layers. The modified form of Arakawa's scheme described here includes the effects of precipitation-cooled downdrafts. The second scheme is based on the boundary-layer quasi-equilibrium scheme used by Emanuel (1995a), but differs from the original Emanuel scheme in certain important details as described in section (g) below. The third scheme, like Ooyama's scheme, assumes that the (net) cloud-base mass flux is proportional to the resolved-scale vertical velocity at the top of the boundary layer, but it includes also the effects of precipitation-cooled downdrafts. In fact, the only difference between the three schemes as implemented here lies in

the closure assumption that determines the cloud-base mass flux.

a. The basic scheme

The exchange of mass between a deep convective cloud and its environment within a grid column, and the exchange between adjacent grid columns is shown schematically in Fig. 2, again for the case of two-dimensional flow in the $x - \sigma$ plane. For the purpose of illustration only, all the mass exchange between adjacent grid cells is taken to occur through the boundary on the right of the grid column ($x = \Delta x$) and we consider the case in which the dependent variables are horizontally staggered with u_n stored on the boundary and other variables in the middle of a grid cell. In the present model, where the variables are not horizontally staggered, the configuration shown would apply to two adjacent gird columns. The subgrid-scale vertical transports are formulated by considering the cloudy and clear-air regions of the grid column separately. The subgrid-scale fluctuations in the dependent variables are associated with different (uniform) values of these quantities in these regions. *Deep convection is assumed to occur in a grid column if the moist static energy in the boundary layer h_b exceeds the saturation moist static energies in the upper and lower troposphere, h_1^* and h_3^** (henceforth, a star denotes the saturation value of a thermodynamic variable). The vertical mass transfer between parts of grid cells is characterized by a mass flux per unit area with magnitude $M = |p^*\langle\dot{\sigma}\rangle/g|$ and units $\mathrm{kg\,s^{-1}\,m^{-2}}$. The positive sign of M is different in different parts of a grid box as indicated in Fig. 2. The resolved-scale averaged mass fluxes $\overline{M}_n$ at levels 2 and 4 are assumed to be positive for ascending motion.

b. The cloud model

As in Arakawa and Ooyama's formulation, the three schemes described here are based upon a steady-state bulk cloud model, indicated by the cloud on the left of the diagram in Fig. 2. In the cloud model, M_{c4} is the cloud-base mass flux from the boundary layer to the middle layer, M_e is mass flux entrained into the cloud from the middle layer, and M_{c2} is the mass flux transferred from the middle layer to the upper layer inside the cloud (here a subscript "c" denotes a cloud property). Continuity of mass requires that

$$M_{c2} = M_{c4} + M_e. \qquad (16)$$

Following Ooyama (1969) we assume that air that detrains from the cloud into layer 1 has zero buoyancy so that, although it is saturated, its temperature is the same as that of the environment in layer 1. Then

$$M_{c2}h_{c1} = M_{c4}h_b + M_e h_3, \qquad (17)$$

where $h_{c1} = h_1^*$ is the saturation moist static energy of

cloudy air in layer 1. As shown below, Eq. (17) determines the mass flux entrained into the cloud.

Combining (16) and (17), and writing

$$M_{c2} = \eta M_{c4}, \tag{18}$$

we obtain

$$\eta = 1 + \frac{h_b - h_1^*}{h_1^* - h_3} \tag{19}$$

and it follows using Eq. (16) that

$$M_e = (\eta - 1)M_{c4}. \tag{20}$$

Note that the condition for deep convection ($h_b > h_1^*$) ensures that the entrainment mass flux given by Eq. (20) is positive, provided that $h_1^* > h_3$; that is, the atmosphere is stable with respect to middle-level convection. This condition is always satisfied in the present calculations.

c. Subgrid-scale mass fluxes in the clear air

It is assumed that precipitation falls into the cloud environment in layer 3 and that a precipitation-cooled downdraft brings air with the moist static energy of that layer into the boundary layer. Let M_{d4} be the downdraft mass flux from the middle layer to the boundary layer. Following Emanuel (1995a) we take the downdraft mass flux proportional to the updraft mass flux, that is,

$$M_{d4} = \chi M_{c4}, \tag{21}$$

where the quantity χ is linked to the precipitation efficiency ε through the expression $\chi = 1 - \varepsilon$. Emanuel (1995a) relates ε to the relative humidity of the middle layer in a way that downdrafts are stronger when the middle layer is relatively dry and weaker when it is relatively moist. For a similar reason we define $\varepsilon = q_3/q_3^*$, where q_3^* is the saturation specific humidity in layer 3. Note that $0 \leq \chi \leq 1$.

Since the grid-averaged vertical velocity at each level is the sum of the average cloud and cloud environment mass fluxes within the grid box, the mass fluxes at levels 2 and 4 in the cloud environment are $M_{c2} - \overline{M}_2$ and $M_{c4} - \overline{M}_4$, respectively. The latter may be subdivided into an amount M_{d4} that occurs in precipitation and an amount $M_{e4} = M_{c4} - M_{d4} - \overline{M}_4$ that occurs in clear air (see Fig. 2). Then, in the cloud-free environment in unit time, $M_{c2}h_{c1}$ units of h are detrained from the cloud to layer 1 and $(M_{c2} - \overline{M}_2)h_2$ units are transferred from this layer to layer 3 by the return circulation associated with the clouds. Altogether, $(M_{e4}h_4 + M_{d4}h_3)$ units of h are transferred from the middle layer to the boundary layer, partly as subsidence in precipitation-free air (the first term in this expression) and partly in precipitation-cooled downdrafts (the second term). Note that (*saturated*) *downdrafts in our model have a larger effect on the boundary layer moist static energy budget per unit mass transferred than subsidence in precipitation-free air, as the origin of downdraft air is higher and the moist static energy lower.* This is different from Eman-

uel's 1989 and 1995 formulations, where the moist entropy of downdraft air and subsiding clear air are the same. It is important to note that, while in many circumstances the precipitation-free, intracloud air will be subsiding (i.e., $M_{e4} > 0$), this does not have to be the case and we shall show that regions of ascent may and do occur (i.e., $M_{e4} < 0$).

d. Subgrid-scale heat and moisture sources

The six equations governing the convection scheme consist of prognostic equations for the dry static energy, $s (= c_p T + \Phi)$, and q in each layer. Then the moist static energy, $h = s + Lq$. The formulation of the equations is essentially the same as that given by Arakawa (1969) and reproduced in the book by Haltiner (1971, see section 10.4), although both authors focus on the closure for middle-level convection, the conditions for which are never met in our model. The basis of the derivation is sketched briefly in appendix c. The assumption that the fractional coverage of convective cloud, μ, in a grid column is small compared with unity enables the grid-averaged changes of these quantities to be approximated with the changes that occur in the cloud environment. Because the grid-scale and subgrid-scale vertical mass fluxes at any level are not independent (see section 3c), the formulation of the source terms and vertical advection terms in Eqs. (7) and (8) need to be considered together wherever deep convection is called for in a grid column. Application of the volume-averaged conservation equation derived in appendix c and the assumption that the cloud-environment mean of q and s is approximately equal to the mean over the entire grid cell leads to the following equations for the rates of change of q and s in the top, middle, and boundary layer as a result of subgrid-scale fluxes:

$$\alpha_1 p^* \frac{\partial q_1}{\partial t} = M_{c2}(q_{c1} - q_1)$$
$$- (M_{c2} - \overline{M}_2)(q_2 - q_1), \tag{22}$$

$$\alpha_3 p^* \frac{\partial q_3}{\partial t} = (M_{c2} - \overline{M}_2)(q_2 - q_3) - M_{d4}(q_{d4} - q_3)$$
$$- (M_{c4} - M_{d4} - \overline{M}_4)(q_4 - q_3), \tag{23}$$

$$\alpha_b p^* \frac{\partial q_b}{\partial t} = M_{d4}(q_{d4} - q_b)$$
$$+ (M_{c4} - M_{d4} - \overline{M}_4)(q_4 - q_b), \tag{24}$$

$$\alpha_1 p^* \frac{\partial s_1}{\partial t} = -(M_{c2} - \overline{M}_2)(s_2 - s_1), \tag{25}$$

$$\alpha_3 p^* \frac{\partial s_3}{\partial t} = (M_{c2} - \overline{M}_2)(s_2 - s_3) - M_{d4}(s_{d4} - s_3)$$
$$- (M_{c4} - M_{d4} - \overline{M}_4)(s_4 - s_3), \tag{26}$$

$$\alpha_b p^* \frac{\partial s_b}{\partial t} = M_{d4}(s_{d4} - s_b)$$

$$+ (M_{c4} - M_{d4} - \overline{M}_4)(s_4 - s_b), \qquad (27)$$

where q_{c1} is the specific humidity of cloudy air in layer 1; s_{d4} and q_{d4} are the dry static energy and specific humidity of downdraft air as it crosses level 4; $\alpha_n = \Delta\sigma_n/g$, where $\Delta\sigma_n$, $(n = 1, 3, b)$ are the thicknesses of layers 1, 3, and b in terms of σ; and s_2, s_4, q_2, q_4 are obtained from values of s and q at adjacent levels by interpolation (the details are explained in appendix b). We have included the grid-scale vertical fluxes in these equations to emphasize that they determine the *net* vertical motion in the cloud environment, but they, together with the grid-scale horizontal transports, are calculated in Eqs. (7) and (8) and the subgrid-scale increments to q and s are calculated from Eqs. (22)–(27) with the grid-scale vertical mass transports excluded.

The heating contributions from deep convection to Q_θ in Eq. (7) are obtained by calculating the increments in dry static energy, Δs_n, during a time step, using Eqs. (25)–(27) with the terms involving the grid-scale mean quantities $\overline{M}_2$ and $\overline{M}_4$ excluded. Then we set $Q_{\theta n} = \Delta s_n/(c_p \pi_n)$, where π_n is the Exner function at the appropriate σ level $(n = 1, 3, b)$. The moistening contributions Q_q in Eq. (8) are obtained in a similar way using Eqs. (22)–(24). When downdrafts are excluded, Eqs. (22)–(27) are identical to those given by Arakawa (1969).

It remains now to calculate the values of s_{d4}, q_{d4}, and M_{c4}. The calculation of s_{d4} and q_{d4} is described in section 3e below. A closure assumption is required to determine the cloud-base mass flux M_{c4}. The three methods explored here are described in sections 3f–3h.

e. Downdraft thermodynamics

The calculation of s_{d4} and q_{d4} is indicated schematically in Fig. 3. It is assumed that rain falls into the air in layer 3 and partially evaporates until the air at this level becomes saturated and cooled to the wet-bulb temperature T_{w3}. Then it is assumed that the cooled air descends into the boundary layer as rain continues to evaporate into it so as to just keep it saturated. The wet-bulb temperature at level 4, T_{w4}, is calculated by solving iteratively the equation

$$c_p T_{w4} + gz_4 + Lq^*(T_{w4}, p_4) = h_3, \qquad (28)$$

and the specific humidity at level 4, q_{w4}, is simply equal to $q^*(T_{w4}, p_4)$. Since the moist static energy of an air parcel is approximately conserved when liquid water evaporates into it as well as during saturated descent, downdrafts reduce the moist static energy of the boundary layer. Further, because the moist static energy of downdraft air at level 4 is less than that of precipitation-free air at this level, downdraft air is more effective in decreasing the boundary layer moist static energy than subsidence in precipitation-free air. This representation of downdrafts leads to the coldest boundary layer temperature that can be achieved by precipitation-cooled subsidence. In reality the evaporation of precipitation is normally insufficient to keep downdrafts saturated, and this diminishes their cooling and moistening effect.

f. The modified 1969 Arakawa scheme

The closure for this scheme is obtained by assuming that deep convection tends to reduce the instability on the timescale, τ_{dc}, and in doing so drives the moist static energy of the upper layer toward that of the boundary layer. Mathematically we write

$$p^* \frac{\partial}{\partial t}(h_b - h_1^*) = -\frac{p^*(h_b - h_1^*)}{\tau_{dc}}. \qquad (29)$$

It can be shown that (see, e.g., Haltiner 1971, p. 189)

$$p^* \frac{\partial}{\partial t}(h_b - h_n^*) = p^* \frac{\partial}{\partial t}(h_b - (1 + \gamma_n)s_n),$$

$$(n = 1, 3, b), \qquad (30)$$

where

$$\gamma_n = \frac{L}{c_p}\left(\frac{\partial q_n^*}{\partial T}\right)_{T_n}. \qquad (31)$$

Then Eq. (29) can be written as

$$\alpha_b p^* \frac{\partial}{\partial t}[h_b - (1 + \gamma_1)s_1] = \frac{-\alpha_b p^*(h_b - h_1^*)}{\tau_{dc}}. \qquad (32)$$

Since $h_b = s_b + Lq_b$, Eqs. (24), (25), and (27), can be used to eliminate the time derivatives in Eq. (32) and the resulting equation provides an expression for the mass flux M_{c4}:

$$M_{c4} = \frac{-\alpha_b p^*(h_b - h_1^*)/\tau_{dc}}{[\chi h_{d4} + (1 - \chi)h_4 - h_b - \eta(\alpha_b/\alpha_1)(s_1 - s_2)(1 + \gamma_1)]}. \qquad (33)$$

Following Arakawa, τ_{dc} is set equal to 1 h. This closure on the cloud-base mass flux is essentially the same as that used in the current version of the European Centre for Medium-Range Weather Forecasts's Integrated Fore-

casting System (Gregory et al. 2000). Indeed, Eqs. (33) is analogous to Eq. (6) of Gregory et al. since $(h_b - h_1^*)$ is a measure of the degree of convective instability between the boundary layer and upper layer and is there-
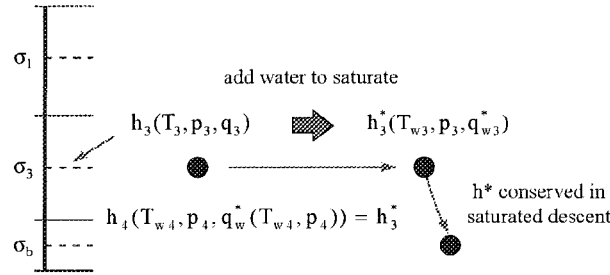
FIG. 3. Schematic diagram showing how the downdraft temperature is determined. First, water is added to air parcels at level 3 until they are saturated. This lowers the temperature to the wet-bulb temperature T_{w3}, but increases the specific humidity to q_{w3}^*. It is assumed then that the parcels descend as precipitation continues to evaporate into them to keep them just saturated. The saturation moist static energy is approximately conserved during this descent.

fore related to the convective available potential energy in our model. Note that both updrafts and downdrafts contribute to the stabilization of their environment as expressed by Eq. (33).

g. The modified 1995 Emanuel scheme

An alternative to the Arakawa closure is that implemented by Emanuel (1995a), who made the assumption that the boundary layer is in quasi-equilibrium (Raymond 1995). Based on this assumption one can derive a prognostic equation for the saturation moist entropy at the top of the subcloud layer (the subcloud layer is taken to be identical to the boundary layer). Emanuel characterizes the thermal structure of the free troposphere by assuming that the (reversible) saturation moist entropy is constant along an absolute angular momentum surface emanating from the boundary layer, equal to its value at the top of this layer. In other words, the free troposphere is assumed to be slantwise neutral[2] to moist convection. Emanuel's model is axisymmetric and the implementation of the foregoing assumption is elegantly facilitated by choosing potential radius as radial coordinate. The use of potential radius coordinates obviates the need to explicitly include an outflow layer in the upper troposphere. In the present three-dimensional model, the use of potential radius is impractical. Accordingly we use Emanuel's method to determine the cloud-base mass flux, but Arakawa's formulation to determine the convective heating and moistening. The latter are not treated separately in Emanuel's formulation so that a separate water budget, and for example the precipitation rate, cannot be determined.

Strict boundary layer equilibrium would require that the sea surface entropy flux is exactly balanced by the flux of low entropy air brought down into the boundary layer by subsidence in precipitation-free air, by precipitation-cooled downdrafts, and by the horizontal entropy

---

[2] Neutral with respect to a *reversible* moist adiabat.

TABLE 1. List of numerical experiments described in this paper.

Experiment	Cumulus convection scheme
1	No convection scheme—grid-scale precipitation only
2	Modified Arakawa scheme
3	Modified Emanuel scheme
4	Modified Ooyama scheme

advection. Then, the local rate of change of boundary layer entropy is zero. In our model we assume that the local rate of change of moist static energy in the boundary layer is zero. The total rate of change of this quantity is obtained by taking $L \times$ Eq. (24) + Eq. (27) and including the surface flux and horizontal advection terms, whereupon

$$\alpha_b p^* \frac{D_h h_b}{DT} = F_{SH} + LF_q + M_{d4}(h_{d4} - h_b)$$
$$+ (M_{c4} - M_{d4} - \overline{M}_4)(h_4 - h_b), \quad (34)$$

where $D_h/Dt = \partial/\partial t + \mathbf{u}_b \cdot \nabla$ denotes the horizontal part of the material derivative, and $\mathbf{u}_b = (u_b, v_b)$. The equilibrium updraft mass flux, M_{c4}^*, is determined from Eq. (34) by assuming that $\partial h_b/\partial t \equiv 0$, whereupon

$$M_{c4}^* = \frac{F_{SH} + LF_q - \alpha_b p^* \mathbf{u}_b \cdot \nabla h_b - \overline{M}_4(h_4 - h_b)}{h_b - \chi h_{d4} - (1 - \chi)h_4}. \quad (35)$$

Following Emanuel, we assume that the instability associated with the latent and sensible heat fluxes from the sea surface is released over a finite timescale τ, which is taken here to be the same as τ_{dc}. The actual mass flux M_{c4} is determined by the equation

$$\frac{D_h M_{c4}}{Dt} = \frac{M_{c4}^* - M_{c4}}{\tau_{dc}} \quad (36)$$

after which M_{c2} is obtained from Eq. (18) and M_e is obtained from Eq. (20).

h. The modified Ooyama scheme

We examine also a closure similar to the one used by Ooyama (1969), in which the (net) cloud-base mass flux is equal to the resolved-scale mass flux at the top of the boundary layer; that is,

$$M_{c4} = -p^* \overline{\sigma}_4 / [g(1 - \chi)]. \quad (37)$$

A consequence is that there is no subgrid-scale subsidence into the boundary layer except that associated with precipitation-cooled downdrafts (i.e., $M_{e4} \equiv 0$).

4. The numerical experiments

In this paper we describe the results of four experiments on an f plane to compare the different parameterization schemes detailed in section 3. These experiments are listed in Table 1. All calculations begin with the initial conditions given in section 2e. A comprehensive sensitivity study of the model will be presented separately.
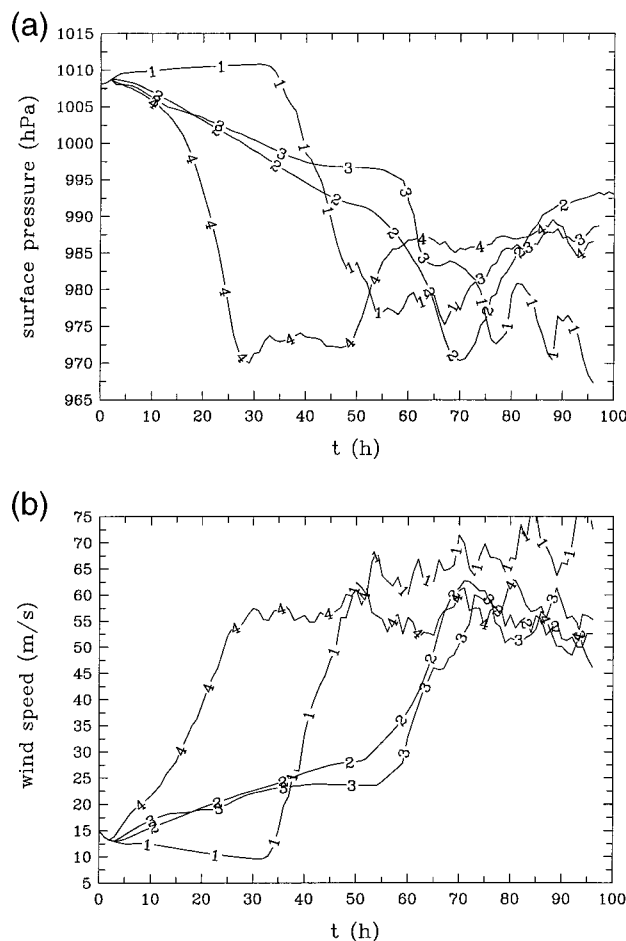
FIG. 4. Variation of (a) minimum surface pressure in mb and (b) maximum total wind speed in m s^{-1} in the lowest layer as a function of time. Numbers on curves refer to experiment numbers in Table 1.

5. Results

a. Overview of vortex evolution

Figure 4 shows time series of the minimum surface pressure and maximum (total) wind speed in the lowest layer for the four experiments listed in Table 1. In broad terms, all the calculations that include a deep cumulus parameterization scheme show a similar pattern of evolution:

- a gestation period during which the vortex gradually intensifies and the central pressure slowly falls,
- a period of rapid intensification and deepening, and,
- a mature stage in which the intensity fluctuates, possible accompanied by a slow mean increase or decline.

This behavior is similar to that in other models and the phenomenon of rapid deepening is well known from observations. According to Pielke and Landsea (1998) it occurs during the formation of most typhoons and all Atlantic hurricanes with wind speeds exceeding 50 m s^{-1} (about 20% of the total). Willoughby (1999) notes

that the onset of rapid deepening is currently unpredictable.

As might be expected, the details of vortex evolution vary with the particular parameterization scheme. In the calculation with only the explicit release of latent heat, the gestation period is replaced by a period of slow decay associated with frictionally induced divergence in the lower troposphere (layer 3). The period of rapid deepening coincides with the occurrence of saturation on the grid scale in level 3. The associated latent heat release creates positive buoyancy in the inner core region. This buoyancy leads to convergence in the lower troposphere, dominating the divergence that would be induced by friction in this region in the absence of significant buoyancy (see, e.g., see section 2 of Smith 2000).

The inclusion of a parameterization scheme for deep cumulus convection leads also to warming and buoyancy-driven convergence in the lower troposphere. Again this convergence exceeds the frictionally induced divergence and accounts for the slow intensification during the gestation period. However, it is significant that even in the three calculations with a parameterization of deep convection, the period of rapid deepening coincides with the explicit release of latent heat in the inner core region (see section 5b). At this stage the vertical temperature profile in an annular region surrounding the core rapidly becomes pseudo–moist adiabatic. Then the condition for parameterized deep convection is no longer satisfied so that the parameterized convection shuts off in this region.

A striking difference between the calculations using different convection schemes is the length of the gestation period: with the Ooyama scheme, this period is quite short with rapid intensification occurring after only about half a day, whereas with the Arakawa and Emanuel schemes it occurs about 2 days later. Perhaps surprisingly, despite the heating produced by parameterized convection, rapid intensification occurs about a day earlier in the case with only explicit moist processes than with the Arakawa or Emanuel parameterization schemes. The reasons for these differences are discussed below. The maximum intensity is similar in all three cases with parameterized convection, but is about 20% smaller than in the calculation with explicit moist processes only, at least for the 96-h duration of the calculations. In all cases the maximum wind speed in the lowest layer exceeds 60 m s^{-1}. At the time of writing we are unable to explain the larger intensity attained when only explicit moist processes are considered and we are investigating this further. Suffice it to say that the maximum tangential wind speed in the boundary layer in the mature stage in experiment 1 is 60 m s^{-1} and in experiments 2–4 it is about 50 m s^{-1} in each case. These values compare with the value 52 m s^{-1} estimated for the maximum potential intensity using Emanuel's theory (Emanuel 1995b).

b. Details of vortex evolution

Many aspects of the vortex evolution can be succinctly illustrated by time–radius plots of selected azimuthally averaged model quantities. Asymmetric flow features that develop during the calculations are considered in section 5c.

Figure 5 shows time–radius plots of the tangential and radial wind components, azimuthally averaged about the domain center at levels 1 and 3, in the calculation with only the explicit release of latent heat. Figure 6 shows similar plots of the perturbation potential temperature (relative to its ambient value) and relative humidity at level 3, as well as the vertical p velocity[3] (ω) at level 4 in this calculation. For about 33 h the initial vortex slowly decays and the radius of maximum tangential wind speed steadily increases (Figs. 5a,b) as a result of frictionally induced radial divergence above the boundary layer (Figs. 5c,d). However, during this period, the specific humidity and relative humidity increase in the boundary layer as a result of the strong surface moisture flux, which increases with wind speed, and also above the boundary layer in the core region as a result of the vertical advection of moisture by the secondary circulation, that is, the azimuthal-mean circulation in the vertical plane. After about 30 h the air at level 3 saturates in the core region (Fig. 6b) and the subsequent latent heat release produces a net[4] positive buoyancy that leads to a brief period of strong convergence at level 3 as seen in Fig. 5d. This inflow is accompanied by strong upflow in an annular region surrounding the core at level 4 (Fig. 6c) and level 2 (Fig. 6d), and strong outflow at level 1 (Fig. 5c). The existence of positive buoyancy[5] is indicated by the perturbation potential temperature distribution shown in Fig. 6a. The pulse in the secondary circulation commences at about 32 h and lasts only a few hours, essentially during the early stages of rapid deepening. Subsequently the inflow declines at level 3 and the inflow maximum slowly extends to larger radii as the vortex itself expands (Figs. 5b,d). With the intensification of the vortex, after about 30 h, the vertical velocity fields at level 4 (Fig. 6c) and level 2 (Fig. 6d) show a region of subsidence along the rotation axis, indicative of an "eye," together with a surrounding annular region of strong ascent, the model analog of eyewall convection. There is an adjacent annular region of subsidence at level 4, beyond

about 90 km in radius, which dries the air in the middle layer (as indicated in Fig. 6b) and in the boundary layer. The region of cooling between about 100 and 200 km radius seen in Fig. 6a is associated with the ascending motion at these radii at level 2.

Salient features of the flow evolution in experiment 2, which incorporates the modified Arakawa parameterization of deep convection, are exemplified by the time–radius plots shown in Figs. 7 and 8. The plots of the tangential and radial wind components, the perturbation potential temperature, and the relative humidity at level 3 are shown in Fig. 7, while Fig. 8 shows the corresponding isolines of convective and explicit precipitation, the calculations of which are detailed in appendix D and in section 2b, respectively. The cooling associated with the boundary layer–forced ascent and moistening due to strong surface moisture fluxes at early times lead rapidly to deep convective instability in the core region and, in contrast to experiment 1, the ensuing subgrid-scale convection progressively warms this region before it saturates on the grid scale (compare the perturbation potential temperature plot in Fig. 7c with that in Fig. 6a). This warming accounts for the slow intensification during the gestation period described in section 5a. The increase in relative humidity by the mean secondary circulation is opposed by drying associated with the intracloud subsidence that accompanies parameterized deep convection (cf. the relative humidity plots in Figs. 6b and 7d). The drying, which occurs at all levels including the boundary layer, delays the onset of grid-scale saturation and thereby the period of rapid development. The amount of drying outside the core region is too large in the mature stage and this appears to be attributable to the inaccurate representation of explicit moisture advection, especially from layer 1 to layer 3.

In the early stages of evolution the precipitation is wholly associated with the convection scheme (Fig. 8a), but as noted earlier, when grid-scale saturation occurs, the parameterization scheme shuts down and the period of rapid deepening begins. Subsequently precipitation occurs predominantly on the grid scale (Fig. 8b). This result is similar to a finding of Baik et al. (1990a), who used the Betts–Miller parameterization scheme in an axisymmetric model with 11 levels in the vertical. Figures 1 and 2 in their paper show at least three periods of rapid intensification, each coinciding with a sharp increase in grid-scale precipitation and a decline in subgrid-scale precipitation.

For the relaxation times chosen, the vortex evolution in experiment 3, which uses the Emanuel parameterization scheme, is very similar to that for the Arakawa scheme and the maximum wind speed attained is almost the same (Fig. 4b).

In experiment 4, which uses Ooyama's scheme, vortex development is even more rapid than in the case with only explicit latent heat release. In this experiment, M_{c4} is much larger than in the other two schemes and the

---

[3] The p velocity $\omega = Dp/Dt = p^*\dot{\sigma} + \sigma(\partial p^*/\partial t + u\partial p^*/\partial x + v\partial p^*/\partial y)$.

[4] A part of the buoyancy distribution is in thermal wind balance, associated with the decay in the tangential circulation with height.

[5] Some care is required in making inferences about buoyancy when using σ coordinates as σ surfaces may have a vertical tilt, and a temperature or potential temperature anomaly on such a surface may be merely a consequence of this tilt. If, for example, the surface pressure falls, so does the pressure on the σ surface and in a stably stratified atmosphere, this implies an increase in potential temperature on that surface, even in the absence of latent heat release. This effect turns out to be relatively small.
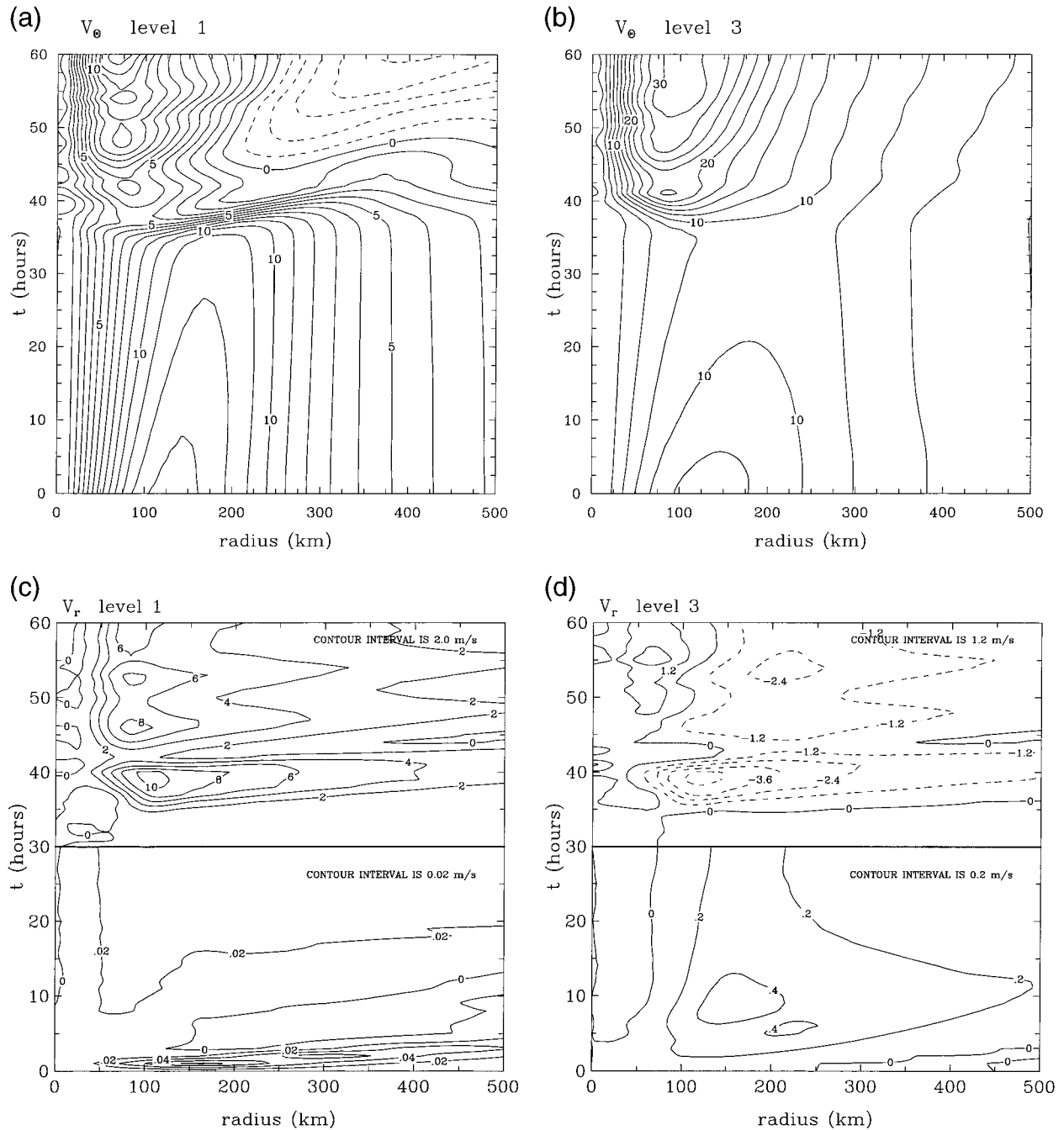
FIG. 5. Time–radius plots of the tangential (v_θ) and radial (v_r) wind components in m s^{-1}, azimuthally averaged about the domain center at levels 1 and 3, in the calculation with only the explicit release of latent heat (experiment 1). (a) Here v_θ at level 1, contour interval is 2 m s^{-1}; (b) v_θ at level 3, contour interval is 2.5 m s^{-1}; (c) v_r at level 1; and (d) v_r at level 3. Dashed lines correspond with negative values. A horizontal line delineates the regions with different contour intervals.

radial distribution is radically different from experiments 2 and 3, with deep convection confined to the inner core region. This is illustrated in Fig. 9, which shows the time–radius plots of M_{c4} for the three calculations that include a parameterization of subgrid-scale deep convection. The larger mass flux implies larger subsidence heating and therefore larger buoyancy whereupon the convergence in

layer 3 is stronger than in experiments 1–3. Moreover, since the convective heating is confined to the core region, where there is boundary layer convergence, the local radial buoyancy gradient is much larger than in experiments 2 and 3 and leads to a stronger secondary circulation in the core region. Of course, the larger subsidence in experiment 4 leads to stronger drying in layer
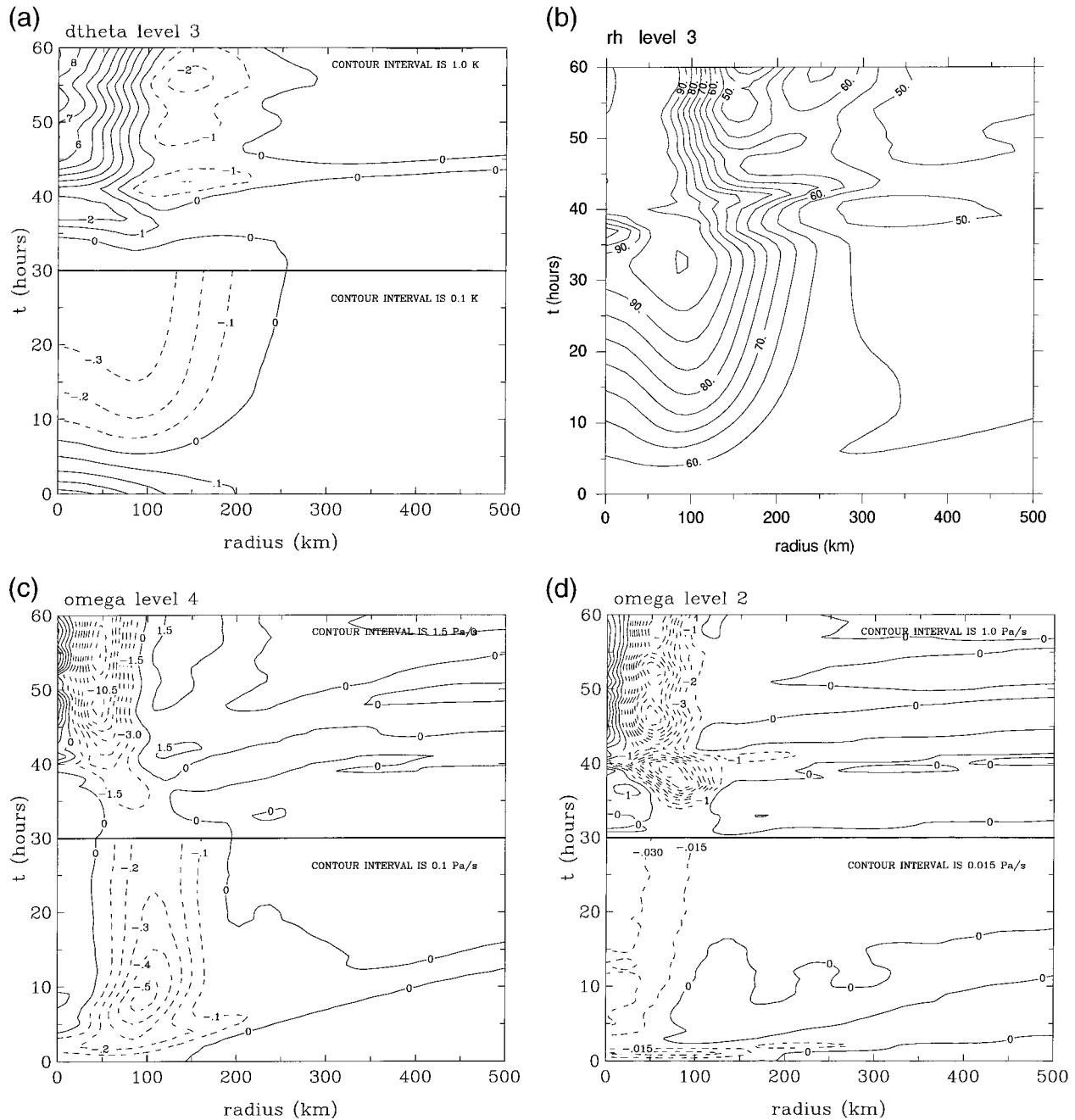
FIG. 6. Legend as for Fig. 5 except for (a) perturbation potential temperature in degrees Kelvin at level 3, (b) relative humidity at level 3 (contour interval 5%), (c) vertical p velocity in Pa s^{-1} at levels 4, and (d) level 2. The contour intervals in (a), (c), and (d) are smaller for $t < 30$ h than for $t > 30$ h as indicated in respective panels.

3, which if acting alone would delay grid-scale saturation in that layer. As it turns out, there are regions of boundary layer convergence and upflow out of the boundary layer where the condition for subgrid-scale deep convection, $h_b > \max(h_3^*, h_1^*)$, is not fulfilled. In these regions, moist boundary layer air is transported upward and quickly leads to grid-scale saturation and rapid deepening. In addition, since *subsidence into the boundary layer is not*

allowed in regions of precipitation-free air in Ooyama's scheme (i.e., $M_{e4} \equiv 0$), there is less drying than in the other schemes and the growth in boundary layer moisture from surface fluxes is therefore more rapid. As a result saturation occurs in the boundary layer after only about 8 h and the latent heat released generates buoyancy and enhances the resolved-scale secondary circulation in this case.
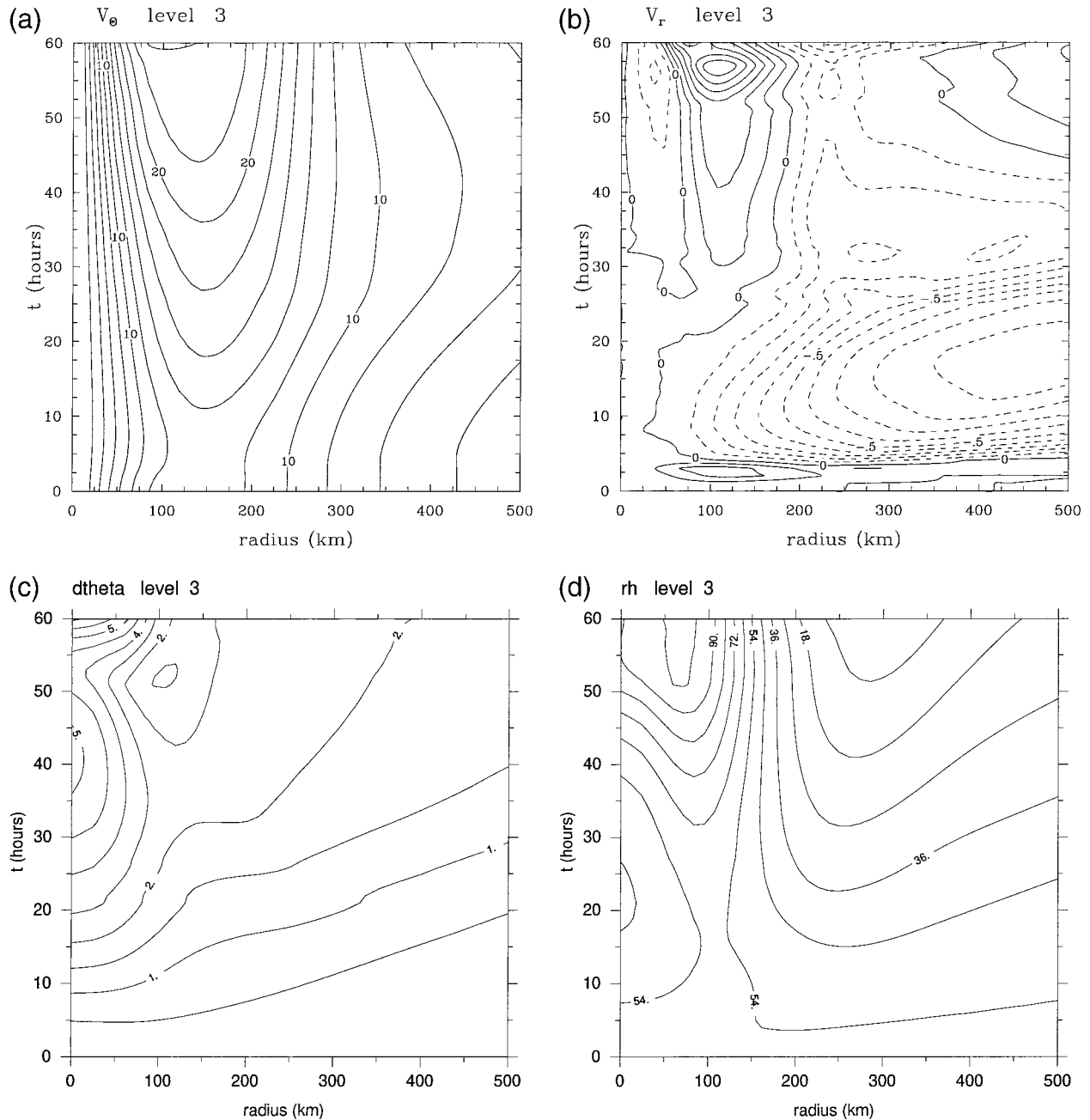
FIG. 7. Legend as for Fig. 5, except for (a) the tangential wind speed (contour interval 2 m s^{-1}), (b) the radial wind speed (contour interval 0.1 m s^{-1}), (c) the perturbation potential temperature (contour interval 0.5 K), and (d) the relative humidity (contour interval 9%), all at level 3 in experiment 2, which uses the modified Arakawa parameterization for deep convection.

The radial distribution of cloud-base mass flux is similar in the calculations with the Arakawa and Emanuel schemes; in these deep convection progressively extends to over 500 km in radius until about 25 h, after which it contracts to the core region (cf. Figs. 9a and 9b). The extension outward accompanies the outward extension of stronger wind speeds, which enhance surface moisture fluxes, and the subsequent retreat is attributable to increased rates of subsidence into the boundary layer,

which reduces the moist static energy of the boundary layer to a level where the conditions for deep convection are no longer fulfilled. The requirement of boundary layer convergence to activate deep convection in the Ooyama scheme precludes this outward extension of deep convection to larger radii, even though the atmosphere becomes unstable at these radii in the sense that $h_b > \max(h_3^*, h_1^*)$. This shortcoming of the Ooyama closure was pointed out by Emanuel (1989, p. 3451).
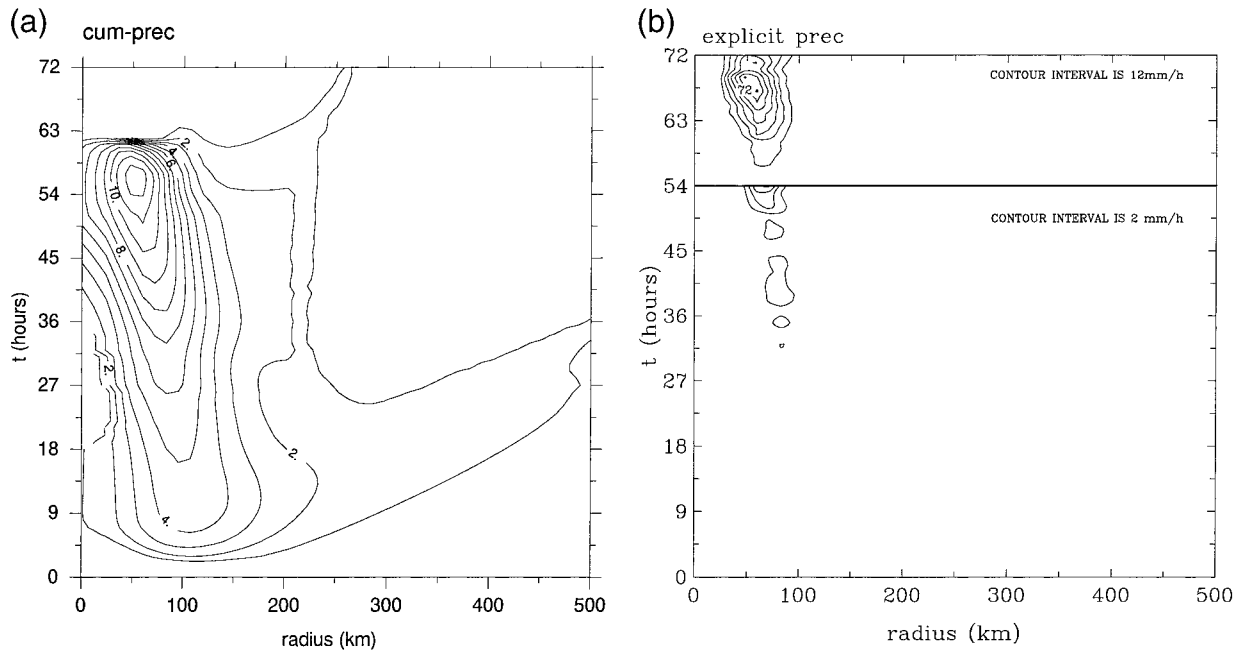
FIG. 8. Legend as for Fig. 5 except for (a) the convective precipitation (contour interval 1 mm h^{-1}), and (b) the explicit precipitation (contour interval 2 mm h^{-1} for $t < 54$ h and 12 mm h^{-1} for $t > 54$ h) in experiment 2.

In comparing the three convection schemes it should be borne in mind that both the Arakawa and Emanuel schemes have adjustable timescales, τ_{dc} and τ, respectively. In Arakawa's scheme, M_{c4} is inversely proportional to τ_{dc} whereas in Emanuel's scheme the dependence of M_{c4} on τ is less direct and weaker. It is significant that in both these schemes, M_{c4} is calculated independently of the large-scale boundary layer convergence. Nevertheless the net heating produced by parameterized convection *does* depend partly on the boundary layer convergence as the latter determines $\overline{M}_4$ and therefore the rate of subsidence (or ascent) in clear air, M_{e4}, through the top of the boundary layer. For example, Fig. 9d shows the time–radius plots of M_{e4} for experiment 2. Note that this quantity is always negative in an annular region between about 50- and 150-km radius; that is, there is always ascent in precipitation-free air in this region. This ascent tends to cool the lower troposphere and is a prerequisite for this layer to moisten. However, it is not sufficient as subsidence may still occur at level 2 and this has a warming and drying tendency, which may dominate the cooling and moistening tendency from ascent at level 4. This is evident, for example, in the relative humidity plot for experiment 2 shown in Fig. 4d. Note that at radii around 100 km, net drying occurs until 16 h, after which time the lower troposphere begins to moisten.

c. Growth of asymmetries

Even though the present calculations are carried out on an f plane and begin with an axisymmetric vortex in an environment at rest, the flow does not remain axisymmetric. Previous calculations in the same flow configuration (e.g., Anthes 1972; Kurihara and Tuleya 1974) show also the evolution of asymmetries, presumably for similar reasons to that here, which are associated with the representation of an axisymmetric flow on a square grid and partly with the use of channel boundary conditions in a domain of finite (albeit relatively large) size. At early times the former effect appears to be the most important as evidenced by its impact on the early location and spatial structure of grid-scale saturation, the pattern of which has an azimuthal wavenumber 4 structure about the vortex center. As the upper-level outflow strengthens and spreads out, it begins to feel the effect of the boundaries and a flow asymmetry with azimuthal wavenumber 2 develops. This asymmetry must be communicated downward to other model levels (of course, a wavenumber 2 asymmetry may be initiated directly at other levels as well). The evolution of the asymmetries is illustrated in Fig. 10, which shows the distribution of $\dot{\sigma}_4$ at the top of the boundary layer (level 4) and the vertical component of relative vorticity at level 3 in experiment 1 at three selected times. A consequence of the wavenumber 4 pattern of grid-scale saturation is that the pattern of upward motion is dominated by the wavenumber 4 asymmetry shortly after saturation occurs (Fig. 10a, upper panel) and the associated vortex-line stretching leads to a quadrupole of mesovortices surrounding the vortex axis (Fig. 10a, lower panel). As the vortex intensifies and matures, these vortices undergo progressive axisymmetrization by the angular shear of the primary vortex as evidenced in the other panels in Fig. 10c. Indeed, already by 42 h, the asymmetries in $\dot{\sigma}_4$
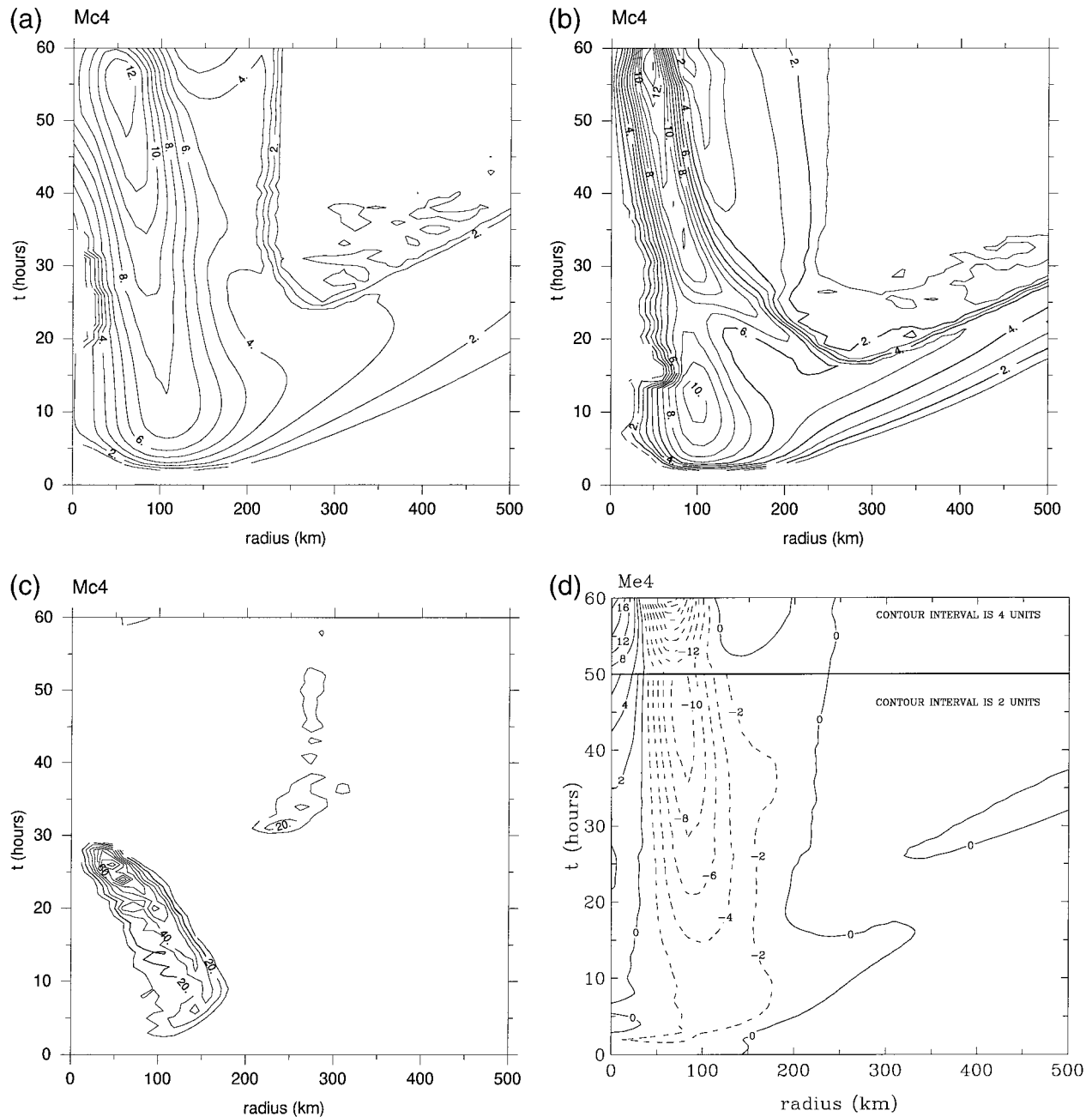
FIG. 9. Legend as for Fig. 5 except for the convective updraft mass fluxes at level 4 (in units 10^{-2} kg m^{-2} s^{-1}). (a) Experiment 2, which uses the modified Arakawa convection scheme (contour interval 1 unit), (b) experiment 3, which uses the modified Emanuel parameterization for deep convection (contour interval 1 unit), (c) experiment 4 which uses the modified Ooyama convection scheme (contour interval 10 units), and (d) the clear airmass flux, M_{e4}, at level 4 in experiment 2 (contour interval 2 units for $t < 50$ h and 4 units for $t > 50$ h).

and ζ are dominated by a wavenumber 2 pattern, which presumably is further strengthened by the effects of boundaries. The process of vortex axisymmetrization has been investigated in the context of idealized barotropic vortices by Smith et al. (1990), Shapiro and Ooyama (1990), and Möller and Montgomery (1999), and in baroclinic vortices by Möller and Montgomery (2000) and Shapiro (2000).

Despite the growth of asymmetries in the model, the vortex evolution cannot be regarded as unrealistic vis-à-vis tropical cyclones. Real storms are always influenced by environmental asymmetries, most likely to a far greater extent than the effect produced by the boundaries in the present model and generally only intense mature storms show convective features that are approximately axisymmetric. One would expect the process of axisymmetrization to be important in reality also.
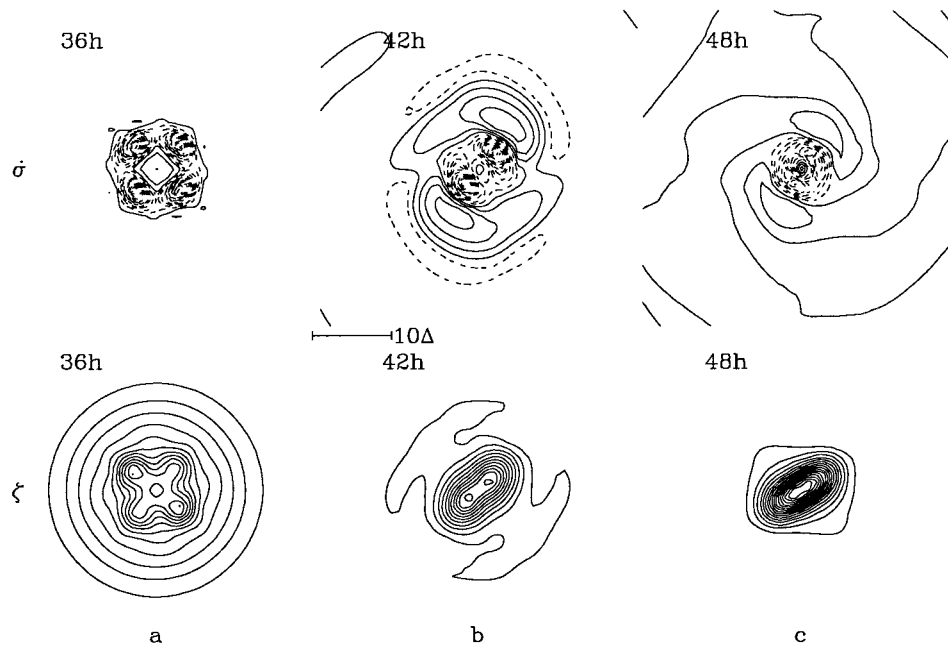
FIG. 10. Patterns of vertical motion characterized by (upper panels) $\dot{\sigma}_4$ and (lower panels) vertical component of relative vorticity at level 3 during the evolution of the vortex in experiment 1 at three selected times: (a) 36 h, (b) 48 h, (c) 60 h. Contour intervals for $\dot{\sigma}_4$ are (a) 5.0×10^{-6} s^{-1}, (b) 1.0×10^{-5} s^{-1}, (c) 2.5×10^{-5} s^{-1}, and for relative vorticity they are 2.0×10^{-5} s^{-1} in (a) and 1.0×10^{-4} s^{-1} in (b) and (c).

6. Discussion

The calculations lead us to hypothesize that the period of rapid development in tropical cyclones is accompanied by a change in the character of deep convection in the inner core region from buoyantly driven, predominantly upright convection to slantwise[6] forced moist ascent. This change in character is presumably what many previous authors consider to be an "organization of convection" by the growing vortex. For example, Ooyama (1969, p. 374) remarks on "the intensification and maintenance mechanism (of tropical cyclones) as a cooperative process between the organized moist convection and the cyclone-scale vortex, a cooperative process between the primary and secondary circulation." Our findings are entirely consistent with this view.

It is interesting also to compare our findings with those of Emanuel (1995a), who conjectures that "the near saturation of a mesoscale column of the troposphere at the cyclone core is a necessary condition for (tropical cyclones) intensification." His argument is that "only when the troposphere is nearly saturated are the downdrafts that normally accompany deep convection suppressed; this allows surface fluxes to actually increase the entropy of the subcloud layer and, through moist

adiabatic adjustment, the temperature of the troposphere." In his model the rate of humidification of the lower troposphere is prescribed in terms of the convective mass flux at cloud base, the entropy difference between the lower troposphere and the boundary layer, and a measure of the relative humidity of the lower troposphere. In our model, on the other hand, intensification begins as soon as the boundary layer becomes unstable to deep convection, which happens within an hour or two. Slow intensification occurs despite the presence of precipitation-cooled downdrafts, but rapid intensification occurs only when a mesoscale column of the troposphere near the cyclone core becomes saturated. In the absence of shallow convection, humidification may occur only when the resolved-scale boundary layer convergence exceeds that which can be accommodated in the updrafts of parameterized convection so that ascent from the boundary layer occurs in clear air. This moisture transport must also be sufficient to oppose the drying effect of subsidence from the upper troposphere. The reasons for the differences between Emanuel's model and ours remain to be explored.

Despite the crude explicit representation of moist processes in the present model, the calculations do raise the question as to what extent it is appropriate to represent moist processes in hurricanes in a way that precludes the occurrence of saturation on the grid scale. For example, the model developed by Emanuel (1989) effectively allows this possibility (neglecting, of course, the difference between a reversible and pseudoadiabat),

---

[6] Although the vertical resolution in the present model is inadequate to properly represent slantwise ascent, we note that the region of ascent at level 2 in experiment 1 is generally broader than that at level 4 and in any case, slantwise ascent is consistent with observations (Jorgensen 1984).

but the more recent scheme (Emanuel 1995a) appears to preclude it.

The present findings may be compared also with those of Wada (1979), who investigated tropical-cyclone evolution in a five-layer axisymmetric, primitive equation model using the Arakawa–Schubert cumulus parameterization scheme. The scheme represents three types of clouds extending the top of a surface-based mixed layer to heights of 5, 9, and 13 km. She refers to these as L(ow)-, M(edium)-, and H(igh)-clouds, respectively. As in our model, she uses a horizontal grid spacing (at least in the inner region) of 20 km, and the Jordan environmental sounding. Her model domain size is 2500 km and she uses a relatively weak initial vortex (maximum tangential wind speed approximately 8 m s^{-1} at a radius of about 130 km). Her model includes also an explicit representation of latent heat release. Wada finds the same three stages of evolution as described in section 5a. At the initial instant, no H clouds exist, but she notes that for the first few hours, M and L clouds appear within a radius of 100 km where there is frictionally induced large-scale upward motion (and, we suggest, large surface moisture fluxes), and these subsequently spread out to radii up to 300 km during the gestation period (presumably as the vortex intensifies and therefore surface moisture fluxes destabilize the atmosphere to convection). The period of rapid intensification in her calculation is accompanied by strong convective activity of H and M clouds near the storm center. Unfortunately she does not give details of the explicit release of latent heat, but she does note (on p. 515) that moistening occurs inside a radius of 200 km where large-scale upward motion occurs. Even so, any grid-scale saturation occurs at most[7] in the upper troposphere (see Figs. 8d and 9d of her paper). Indeed the grid-scale relative humidity in the lower troposphere is only on the order of 50%, even in the innermost 100 km, during the period of rapid intensification and falls even lower during the mature stage. The drying is clearly associated with the intra-cloud subsidence in regions of strong convection and this evidently precludes grid-scale saturation in the lower troposphere. We may surmise that parameters in Wada's model are such that the frictionally induced ascent in the core region is always less than the M and H clouds are able to accept (i.e., in our notation, M_{e4} is always positive). Finally recall that the Arakawa–Schubert convection scheme used in Wada's model makes the same small fractional area of cloud assumption as in ours.

7. Model appraisal

The development of the present model has been motivated by the desire to isolate the minimum components required to produce a realistic hurricane-like vortex in a three-dimensional configuration with a fully integrated (albeit highly simplified) representation of moist physics. The benefits of such a model are that it may be simple enough to provide insights into some aspects of the complex interactions that occur between moist convection and the larger-scale vortex circulation in a variety of situations. Inevitably, simplicity is achieved at the expense of accuracy in the quantification of some processes. The hope is that the levels of inaccuracy do not affect the broad conclusions that are drawn from the model, but the extent to which this is the case may only be fully checked by a comparison with results of similar calculations using more complex models. Some specific limitations of the current model are considered below.

1) The representation of explicit latent heat release as a pseudoadiabatic process is an extreme oversimplification and will overestimate the buoyancy in the inner core convection during the rapidly developing stage through its neglect of water loading and mixing with the environment, except for the mixing due to model diffusion. However, the fact that the peak intensity of the model vortex is reasonable implies that the buoyancy distribution produced by the explicit release of latent heat is also within a range that is reasonable.

2) It might be argued that, on account of the nonlinear variation of specific humidity with pressure (or σ) in the tropical atmosphere, the vertical advection of water vapor may be subject to large error in a model with only three vertical layers as used here. This may be an issue during the relatively short period of time that a grid column takes to saturate, but when saturation is achieved, all that matters is that the thermodynamic profile within the column is close to a moist adiabat with $h_b = h_3^* = h_1^*$. This state is achieved by the present scheme.

3) The time at which grid-scale saturation occurs can be expected to be a function of the horizontal and vertical resolution. Indeed, a calculation similar to experiment 1 in which the grid spacing was halved to 10-km reduced the onset time of rapid deepening by about 12 h. The dependence on horizontal resolution in particular must be a concern of *all* models that incorporate both explicit and implicit representations of moist physics and especially those that are designed with a view to forecasting tropical-cyclone intensity change. A calculation similar to experiment 1 with five vertical layers showed also a reduction in the time of grid-scale saturation and the onset of rapid deepening by about 10 h. An in-depth discussion of the issues involved in representing moist processes on the mesoscale is the subject of review papers by Molinari and Dudek (1992) and Kuo et al. (1997).

4) It would be more realistic to allow subgrid-scale convection to transfer momentum vertically.

5) Convective downdrafts are generally unsaturated and lower the moist static energy of the boundary layer

---

[7] The highest contour level shown for relative humidity is 90%.

(Betts 1976, p. 1019). Thus our downdrafts are too moist and too cold, but their qualitative effect on the moist static energy of the boundary layer would not change if a degree of subsaturation were allowed.

6) All the convection schemes considered here are based on a steady-state cloud model that transports boundary layer air to the upper troposphere. In reality, as convective systems mature, they develop a different mean structure in which there is mesoscale subsidence in the lower troposphere and mesoscale ascent in the upper troposphere. In a more complete theory, this change in structure ought to be taken into account (see, e.g., Betts 1997).

7) The convection schemes assume that convective updrafts occupy only a small fraction of a grid column, whereas explicit convection occurs only when an entire grid cell is saturated. The gap between these two extreme situations needs to be filled.

8) It might be a little more realistic to initialize the calculations with a baroclinic vortex somewhat weaker than the one used here, although many authors have chosen an initial vortex similar in strength to ours as this enhances the surface energy fluxes and thereby reduces the gestation period (and hence the computational time).

9) The present model does not include the effects of shallow convection, which would moisten and cool the middle layer and warm and dry the boundary layer, besides exchanging horizontal momentum between these layers.

These are all factors that need to be explored in future investigations.

8. Summary and conclusions

We have developed a minimal three-dimensional numerical model for a tropical cyclone in which dynamical and thermodynamical processes are closely interlinked through explicit and parameterized representations of moist processes. Like most other models, the present one is capable of simulating the development of a mature hurricane-like vortex from an existing vortex of tropical depression intensity in a maritime environment where the sea surface temperature is high. In our case, the environment is slightly *stable* to deep cumulus convection at the initial instant.

Vortex intensification is characterized by a gestation period of between half a day and two and one-half days, depending on which cumulus parameterization scheme is implemented, followed by a period of rapid intensification lasting on the order of 12 h. Intensification occurs irrespective of the implementation of a cumulus parameterization scheme and in all calculations, the period of rapid deepening begins when grid-scale saturation occurs in the inner core region. With the modified Arakawa or Emanuel parameterization schemes, in which the cloud-base mass flux of deep convection is unrelated to the boundary layer

convergence, the period of rapid intensification begins later than in the cases with explicit convection only, or with the modified Ooyama scheme. While deep convection produces enhanced buoyancy in the inner region in the early stages of development, the associated intra-cloud downdrafts not only warm, but also dry the boundary layer and middle troposphere. The drying delays the time at which saturation occurs on the grid scale and opposes the convective destabilization of the boundary layer caused principally by surface moisture fluxes in regions of strong boundary layer wind speeds. With the Ooyama scheme, some boundary layer convergence occurs in a region where the atmosphere is conditionally stable and the associated moistening of the lower troposphere leads rapidly to saturation on the grid scale. As a result, the period of rapid intensification begins earlier than in the case with explicit convection only.

Details of the vortex evolution depend on the particular parameterization scheme chosen to represent deep convection and the parameters therein (essentially the relaxation time in the Arakawa and Emanuel schemes), as well as other model parameters such as the horizontal grid resolution and the choice of layer depths. A study of the model sensitivity to the various parameters will be submitted for publication in due course.

Although the present calculations are carried out on an f plane and begin with an axisymmetric vortex, the vortex does not remain axisymmetric as is found in other studies. We attribute the growth of an azimuthal wavenumber 4 component of asymmetry to the representation of a circular flow on a rectangular grid and a wavenumber 2 component to the use of a rectangular domain with channel boundary conditions. The wavenumber 4 component first becomes pronounced when saturation occurs on the grid scale and the wavenumber 2 component appears later as the outflow starts to feel the boundaries. Subsequently the asymmetry in the inner vortex core tends to decline on account of the strong angular shear of the mean tangential circulation through the well-known process of vortex axisymmetrization. While the initiation of the asymmetries in the model may not be realistic vis-à-vis tropical cyclones, the processes involved in their subsequent evolution are probably quite realistic.

APPENDIX A

The Initial Sounding Data

TABLE A1. The initial pressure (p), temperature (T), specific humidity (q), and geopotential height (Φ) in the middle of each layer and at the boundaries between layers in the far field.

σ	p (mb)	q (g kg^{-1})	T(K)	Φ (m^2 s^{-1})
$\sigma_1 = 1/6$	252.5	0.01	230.4	106 549
$\sigma_2 = 1/3$	405.0	0.15	256.1	73 557
$\sigma_3 = 11/18$	659.2	4.82	278.9	36 066
$\sigma_4 = 8/9$	913.3	13.6	293.8	9098
$\sigma_b = 17/18$	964.2	13.9	297.0	4461

APPENDIX B

Some Details of the Numerical Method

The Adams–Bashforth third-order scheme is used with a time step of 15 s, that is,

$$U^{(n+1)} = U^{(n)} + \left(\frac{23}{12}F^{(n)} - \frac{16}{12}F^{(n-1)} + \frac{5}{12}F^{(n-2)}\right)\Delta t,$$

where the $F^{(n)}$ are the tendencies of $U^{(n)}$. Horizontal (x, y)-plane derivatives are evaluated on a nonstaggered grid. Second-order finite differences are used in all runs. The standard advection scheme uses third-order upwinding based on standard third-order approximations for the derivatives, which involve four grid points with two in the upwind direction and one in the downwind direction.

We adopt the method of Arakawa and Suarez (1983) for the vertical difference scheme and the hydrostatic equation. For convenience, we use half-integer subscripts $1/2, 1+1/2, 2+1/2, 3+1/2$ to represent the top level ($\sigma = 0$), the two interface levels, and the bottom level ($\sigma = 1$). The increment in σ is given by

$$\Delta\sigma_k = \sigma_{k+1/2} - \sigma_{k-1/2}.$$

For any variable A that is carried at the kth level, the flux form can be written:

$$\frac{\partial(p^*A_k)}{dt} + \nabla \cdot (p^*A_kV_k)$$
$$+ \frac{1}{\Delta\sigma_k}[(p^*\dot\sigma)_{k+1/2}\hat A_{k+1/2} - (p^*\dot\sigma)_{k-1/2}\hat A_{k-1/2}] = 0.$$

This form guarantees that the global average of A will be conserved as a result of advection. This equation can be rewritten in advection form using the continuity equation, which is consistent with the flux form and gives the expression:

$$\left(\frac{\partial}{\partial t} + V_k \cdot \nabla\right)A_k$$
$$+ \frac{1}{\Delta\sigma_k p^*}[(p^*\dot\sigma)_{k+1/2}(\hat A_{k+1/2} - A_k)$$
$$+ (p^*\dot\sigma)_{k-1/2}(A_k - \hat A_{k-1/2})] = 0.$$

In the case of wind speed and specific humidity we define A at the interface levels as

$$\hat A_{k+1/2} = (A_k + A_{k+1})/2.$$

In the case of potential temperature, we define

$$\hat\theta_{k+1/2} = \frac{(\hat P_{k+1/2} - P_k)\theta_k + (P_{k+1} - \hat P_{k+1/2})\theta_{k+1}}{P_{k+1} - P_k},$$

$$\hat P_{k+1/2} = \left(\frac{\hat p_{k+1/2}}{p_0}\right)^\kappa, \quad \text{and}$$

$$P_k = \frac{1}{1+k}\left[\frac{\hat P_{k+1/2}\hat p_{k+1/2} - \hat P_{k-1/2}\hat p_{k-1/2}}{\hat p_{k+1/2} - \hat p_{k-1/2}}\right],$$

which guarantees that θ is conserved. The interface value for the dry static energy is obtained in the same way as for θ.

The hydrostatic equation is

$$\Phi_b - \Phi_s = c_p\theta_b(P_s - P_b),$$

$$\Phi_k - \Phi_{k+1} = c_p\hat\theta_{k+1/2}(P_{k+1} - P_k).$$

Note the different form for the lowest level.

APPENDIX C

Conservation Equation for Part or All of a Grid Cell

The formulation of the equations for subgrid-scale processes in cloud-free air in the convection scheme is aided by considering the conservation equation for some quantity ϕ. For example, the quantity ϕ might be the dry static energy $s = c_pT + gz$, the specific humidity q, the moist static energy $h = s + Lq$, or a horizontal velocity component. We write the equation in flux form expressed in σ coordinates. It is sufficient to consider the two-dimensional situation in the x–σ plane. The equation for ϕ is

$$\frac{\partial}{\partial t}(p^*\phi) + \frac{\partial}{\partial x}(p^*u\phi) + \frac{\partial}{\partial\sigma}(p^*\dot\sigma\phi) = p^*S_\phi, \quad \text{(C1)}$$

where S_ϕ is the mean rate of generation of ϕ. We define a horizontal average over a cloud-free air interval $\Delta x_{cf} = x_2 - x_1$, denoted by an overbar, and a vertical average over an interval $\Delta\sigma = \sigma_B - \sigma_A > 0$, denoted by $\langle\ (\ )\ \rangle$; that is,

$$\overline{(\ )} = \frac{1}{\Delta x_{cf}}\int_0^{\Delta x_{cf}} (\ )\, dx, \quad \text{and}$$

$$\langle (\ )\rangle = \frac{1}{\Delta\sigma}\int_{\sigma_A}^{\sigma_B} (\ )\, d\sigma. \quad \text{(C2)}$$

In Fig. 2, for example, $x_1 = \mu\Delta x$ and $x_2 = \Delta x$. Applying these integrals in succession to Eq. (C1) and noting that they commute gives

$$\frac{\partial}{\partial t}\langle \overline{p^*\phi}\rangle = -\frac{1}{\Delta x_{cf}}[\langle p^*u\phi\rangle]_{x_1}^{x_2} - \frac{1}{\Delta\sigma}[\overline{p^*\dot\sigma\phi}]_{\sigma_A}^{\sigma_B}$$
$$+ \langle \overline{p^*S_\phi}\rangle. \tag{C3}$$

Putting $\phi = 1$ and $S_\phi = 0$ gives the mass continuity equation for the volume element $\Delta x_{cf}\Delta\sigma$:

$$\frac{\partial}{\partial t}\langle \overline{p^*}\rangle = -\frac{1}{\Delta x_{cf}}[\langle p^*u\rangle]_{x_1}^{x_2} - \frac{1}{\Delta\sigma}[\overline{p^*\dot\sigma}]_{\sigma_A}^{\sigma_B}. \tag{C4}$$

We assume that $\overline{\dot\sigma\phi} = \overline{\dot\sigma}\ \overline{\phi}$, $\langle u\phi\rangle = \langle u\rangle\langle\phi\rangle$, and that p^* is horizontally uniform over the interval Δx_{cf}. Thus sub-grid-scale fluxes are assumed to be zero in the cloud-free air region within a grid box. Then, denoting the volume average of this element by $\widehat{(\ )} = \widehat{\langle(\ )\rangle}$ and subtracting $\hat\phi$ times Eq. (C4) from Eq. (C3) gives

$$p^*\frac{\partial\hat\phi}{\partial t} = -\frac{1}{\Delta x_{cf}}[p^*\langle u\rangle(\langle\phi\rangle - \hat\phi)]_{x_1}^{x_2}$$
$$-\frac{1}{\Delta\sigma}[p^*\overline{\dot\sigma}(\overline{\phi} - \hat\phi)]_{\sigma_A}^{\sigma_B} + p^*\hat S_\phi. \tag{C5}$$

In terms of the vertical mass flux per unit area defined in section 3b, Eq. (C5) takes the form

$$\alpha p^*\frac{\partial\hat\phi}{\partial t} = -\frac{1}{\Delta x_{cf}}[\alpha p^*\langle u\rangle(\langle\phi\rangle - \hat\phi)]_{x_1}^{x_2}$$
$$- [M(\overline{\phi} - \hat\phi)]_{\sigma_A}^{\sigma_B} + \alpha p^*\hat S_\phi, \tag{C6}$$

where $\alpha = (\sigma_B - \sigma_A)/g > 0$.

The term on the left-hand side of Eq. (C6) is the rate of change of the volume average of $\hat\phi$. The first two terms on the right-hand side characterize the change in $\hat\phi$ associated with the mean horizontal flux of $\hat\phi - \phi_{\text{boundary}}$ through the sides of the element and the net vertical flux of $\hat\phi - \phi_{\text{boundary}}$ through the base ($\sigma = \sigma_B$) and top ($\sigma = \sigma_A$) of the element, where ϕ_{boundary} is the value of ϕ at the boundary. Note that these flux terms are zero when the flow is directed out of the volume element. The last term of Eq. (C6) characterizes the mean source of $\hat\phi$ within the element.

In section 3d, Eq. (C6) is used to determine the time rate of change of s and q in the cloud-free regions of cells in a grid column that are deemed to contain deep convective cloud.

APPENDIX D

Calculation of the Cumulus Precipitation

Addition of Eqs. (27), (28), and (29) gives

$$p^*\frac{\partial}{\partial t}(\alpha_1 q_1 + \alpha_3 q_3 + \alpha_b q_b)$$
$$= (M_{c2}q_{c1} - M_e q_3 - M_{c4}q_b) - \overline{M_2}(q_1 - q_3)$$
$$- \overline{M_4}(q_3 - q_b). \tag{D1}$$

The first term on the right-hand side is the rate of loss of water vapor to the deep convective clouds in a grid box. Because the clouds are assumed to be steady, this rate of water loss, minus that consumed in moistening precipitation-driven downdrafts is equal to the convective precipitation rate:

$$-M_{c2}q_{c1} + M_e q_3 + M_{c4}q_b - M_{d4}(q_{d4} - q_3). \tag{D2}$$

The second and third terms on the right-hand side of Eq. (D1) represent the net moisture convergence into a column by the large-scale motion, but these do not represent the explicit precipitation as the net moisture in a column can change.

REFERENCES

Anthes, R. A., 1972: Development of asymmetries in a three-dimensional numerical model of a tropical cyclone. *Mon. Wea. Rev.,* **100,** 461–476.
——, S. L. Rosenthal, and J. W. Trout, 1971a: Preliminary results from an asymmetric model of the tropical cyclone. *Mon. Wea. Rev.,* **99,** 744–758.
——, J. W. Trout, and S. L. Rosenthal, 1971b: Comparisons of tropical cyclone simulations with and without the assumption of circular symmetry. *Mon. Wea. Rev.,* **99,** 759–766.
Arakawa, A., 1969: Parameterization of cumulus convection. *Proc. WMO/IUGG Symp. Numerical Weather Prediction,* Tokyo, Japan, Japan Meteorological Agency, 1–6.
——, and W. H. Schubert, 1974: Interaction of a cumulus cloud ensemble with the large-scale environment Part I. *J. Atmos. Sci.,* **31,** 674–701.
——, and M. J. Suarez, 1983: Vertical differencing of the primitive equations in sigma coordinates. *Mon. Wea. Rev.,* **111,** 34–45.
Baik, J.-J., M. DeMaria, and S. Raman, 1990a: Tropical cyclone simulations with the Betts convective adjustment scheme. Part I: Model description and control simulation. *Mon. Wea. Rev.,* **118,** 513–528.
——, ——, and ——, 1990b: Tropical cyclone simulations with the Betts convective adjustment scheme. Part II: Sensitivity experiments. *Mon. Wea. Rev.,* **118,** 529–541.
——, ——, and ——, 1991: Tropical cyclone simulations with the Betts convective adjustment scheme. Part III: Comparisons with the Kuo parameterization. *Mon. Wea. Rev.,* **119,** 2889–2899.
Betts, A. K., 1976: The thermodynamic transformation of the tropical subcloud layer by precipitation and downdrafts. *J. Atmos. Sci.,* **33,** 1008–1020.
——, 1986: A new convective adjustment scheme. I. Observational and theoretical basis. *Quart. J. Roy. Meteor. Soc.,* **112,** 677–691.
——, 1997: Parameterization of deep convection. *The Physics and Parameterization of Moisture Atmospheric Convection,* R. K. Smith, Ed., Kluwer, 255–279.
DeMaria, M., and J. D. Pickle, 1988: A simplified system of equations for simulating tropical cyclones. *J. Atmos. Sci.,* **45,** 1542–1554.
Elsberry, R. L., 1995: Tropical cyclone motion. *Global Perspectives on Tropical Cyclones,* R. L. Elsberry, Ed., World Meteorological Organization, WMO Tech. Document 693, 106–197.
Emanuel, K. A., 1986: An air–sea interaction theory for tropical cyclones. Part I: Steady-state maintenance. *J. Atmos. Sci.,* **43,** 585–604.
——, 1989: The finite-amplitude nature of tropical cyclogenesis. *J. Atmos. Sci.,* **46,** 3431–3456.
——, 1994: *Atmospheric Convection.* Oxford University Press, 580 pp.
——, 1995a: The behavior of a simple hurricane model using a convective scheme based on subcloud-layer entropy equilibrium. *J. Atmos. Sci.,* **52,** 3960–3968.
——, 1995b: Sensitivity of tropical cyclones to surface exchange

coefficients and a revised steady state model incorporating eye dynamics. *J. Atmos. Sci.,* **52,** 3969–3976.

——, and D. J. Raymond, Eds.,1993: *The Representation of Cumulus Convection in Numerical Models. Meteor. Monogr.,* No. 46, Amer. Meteor. Soc., 246 pp.

——, J. D. Neelin, and C. S. Bretherton, 1994: On large-scale circulations of convecting atmospheres. *Quart. J. Roy. Meteor. Soc.,* **120,** 1111–1143.

Gregory, D., J.-J. Morcrette, C. Jakob, A. C. M. Beljaars, and T. Stockdale, 2000: Revision of convection, radiation, and cloud schemes in the ECMWF Integrated Forecasting System. *Quart. J. Roy. Meteor. Soc.,* **126,** 1685–1710.

Haltiner, G. J., 1971: *Numerical Weather Prediction.* John Wiley and Sons, 317 pp.

Jones, R. W., 1977: A nested grid for a three-dimensional model of a tropical cyclone. *J. Atmos. Sci.,* **34,** 1528–1533.

——, 1980: A three-dimensional tropical cyclone model with release of latent heat by the resolvable scales. *J. Atmos. Sci.,* **37,** 930–938.

Jordan, C. L., 1957: Mean soundings for the West Indies area. *J. Meteor.,* **15,** 91–97.

Jorgensen, D. P., 1984: Mesoscale and convective-scale characteristics of mature hurricanes. Part II: Inner core structure of Hurricane Allen (1980). *J. Atmos. Sci.,* **41,** 1287–1311.

Kuo, H. L., 1965: On the formation and intensification of tropical cyclones through latent heat release by cumulus convection. *J. Atmos. Sci.,* **22,** 40–63.

——, 1974: Further studies of the parameterization of the influence of cumulus convection on large-scale flow. *J. Atmos. Sci.,* **31,** 1232–1240.

——, J. F. Bresch, M.-D. Cheng, J. Kain, D. B. Parsons, W.-K. Tao, and D.-L. Zhang, 1997: Summary of a mini-workshop on cumulus parameterization for mesoscale models. *Bull. Amer. Meteor. Soc.,* **78,** 475–491.

Kurihara, Y., and R. E. Tuleya, 1974: Structure of a tropical cyclone developed in a three-dimensional numerical simulation model. *J. Atmos. Sci.,* **31,** 893–919.

——, and M. A. Bender, 1980: Use of a movable nested-mesh model for tracking a small vortex. *Mon. Wea. Rev.,* **108,** 1792–1809.

Madala, R. V., and S. A. Piacsek, 1975: Numerical simulation of asymmetric hurricanes on an f-plane with vertical shear. *Tellus,* **27,** 453–468.

Molinari, J., and M. Dudek, 1992: Parameterization of convective precipitation in mesoscale numerical models: A critical review. *Mon. Wea. Rev.,* **120,** 326–344.

Möller, J. D., and M. T. Montgomery, 1999: Vortex Rossby waves and hurricane intensification in a barotropic model. *J. Atmos. Sci.,* **56,** 1674–1687.

——, and ——, 2000: Tropical cyclone evolution via potential vorticity anomalies in a three-dimensional balance model. *J. Atmos. Sci.,* **57,** 3366–3387.

Ooyama, K. V., 1969: Numerical simulation of the life cycle of tropical cyclones. *J. Atmos. Sci.,* **26,** 3–40.

Pielke, R. A., 1984: *Mesoscale Numerical Modelling.* Academic Press, 612 pp.

Pielke, R. A., Jr., and C. W. Landsea, 1998: Normalized hurricane damage in the United States 1925–95. *Wea. Forecasting,* **13,** 621–631.

Raymond, D. J., 1995: Regulation of moist convection over the West Pacific warm pool. *J. Atmos. Sci.,* **52,** 3945–3959.

Rosenthal, S. L., 1978: Numerical simulation of tropical cyclone development with latent heat release by the resolvable scales I: Model description and preliminary results. *J. Atmos. Sci.,* **35,** 258–271.

Rotunno, R., and K. A. Emanuel, 1987: An air–sea interaction theory for tropical cyclones. Part II: Evolutionary study using a non-hydrostatic axisymmetric numerical model. *J. Atmos. Sci.,* **44,** 542–561.

Shapiro, L. J., 1992: Hurricane vortex motion and evolution in a three-layer model. *J. Atmos. Sci.,* **49,** 140–153.

——, 2000: Potential vorticity asymmetries and tropical cyclone evolution in a moist three-layer model. *J. Atmos. Sci.,* **57,** 3645–3662.

——, and K. V. Ooyama, 1990: Barotropic vortex evolution on a beta plane. *J. Atmos. Sci.,* **47,** 170–187.

Smith, R. K., Ed., 1997: *The Physics and Parameterization of Moist Atmospheric Convection.* Kluwer, 498 pp.

——, 2000: The role of cumulus convection in hurricanes and its representation in hurricane models. *Rev. Geophys.,* **38,** 465–489.

——, W. Ulrich, and G. Dietachmayer, 1990: A numerical study of tropical cyclone motion using a barotropic model. Part I: The role of vortex asymmetries. *Quart. J. Roy. Meteor. Soc.,* **116,** 337–362.

Wada, M., 1979: Numerical experiments of the tropical cyclone model by use of the Arakawa–Schubert parameterization. *J. Meteor. Soc. Japan,* **57,** 505–530.

Willoughby, H. E., 1999: Hurricane heat engines. *Nature,* **401,** 649–650.

——, H.-L. Jin, S. J. Lord, and J. M. Piotrowicz, 1984: Hurricane structure and evolution as simulated by an axisymmetric, non-hydrostatic numerical model. *J. Atmos. Sci.,* **41,** 1169–1186.

Yamasaki, M., 1975: A numerical experiment of the interaction between cumulus convection and larger scale motion. *Pap. Meteor. Geophys.,* **26,** 63–91.

——, 1977: A preliminary experiment of the tropical cyclone without parameterizing the effects of cumulus convection. *J. Meteor. Soc. Japan,* **55,** 11–30.